UNIVERSITÀ DEGLI STUDI DI PADOVA

UNIVERSITA' DEGLI STUDI DI PADOVA

Department of Industrial Engineering DII

Master of Science in Aerospace Engineering

Aerodynamical analysis of ExoMars capsule during Mach 5 Mars atmospheric descent

Thesis advisor: Prof. Picano Francesco

Thesis co-advisors: Ing. Michele Cogo,

Ing. Luca Placco

Candidate: Giulia Scattola

Registration number: 2026874

Accademic Year 2021/2022

Sommario

L'obiettivo di questo lavoro è l'analisi aerodinamica del campo fluido attorno alla capsula ExoMars durante la fase di rientro atmosferico su Marte. In particolare, viene simulato il flusso caratterizzato da un numero di Mach pari a 5 e i risultati vengono poi confrontati con quelli ottenuti nel caso di Mach 2. L'importanza di questo lavoro è legata alla criticità della fase d'ingresso atmosferico, in cui un singolo inconveniente può portare al fallimento dell'intera missione. Un esempio della criticità di questa fase, denominata Entry, Descent and Landing, è rappresentata dal fallimento della capsula Schiaparelli. Lanciata nel 2016 nell'ambito della prima missione ExoMars, oscillazioni della capsula, legate all'apertura del paracadute, hanno indotto un errore nel sistema di guida e controllo che ha sganciato i paracadute troppo presto. La capsula non è stata rallentata a sufficienza e si è schiantata al suolo[2].
Il lavoro si concentra sulla fase precedente, indicata come Entry phase, nella quale la capsula sfrutta l'attrito atmosferico per rallentare, dissipando energia cinetica, dovuta all'elevata velocità, sotto forma di energia termica. In particolare si osserva il caso in cui la velocità risulta essere cinque volte quella del suono, che su Marte vale 257 m/s e la capsula è parallela al flusso (angolo d'attacco pari a 0°). In questa fase si ha la formazione di un onda d'urto curva distaccata davanti la capsula e di una scia turbolenta nella parte di flusso posteriore. L'analisi condotta interessa entrambi i fenomeni.
La tecnica utilizzata in questo studio prende nome di Implicit Large-Eddy Simulation e prevede la simulazione dei soli vortici più grandi presenti nella zona turbolenta mentre il contributo dei vortici più piccoli viene assimilato agli effetti dissipativi intrinseci degli schemi numerici adottati. Così facendo, è possibile trattare i flussi ad elevato Reynolds e ricostruire puntualmente la scia turbolenta che si forma dietro la capsula. Il solutore scelto è STREAmS, sviluppato all'Università la Sapienza di Roma [10]. Questo, sfruttando la tecnica DMS, implementa una formulazione ibrida tra schemi conservativi e ricostruzioni WENO, in modo tale da trattare in maniera ottimale i campi fluidodinamici che presentano discontinuità e regioni turbolente.
Il primo capitolo fornisce il contesto all'interno del quale questo lavoro si pone, presentando in breve la missione ExoMars, la storia legata allo sviluppo della geometria della capsula, una descrizione della fase d'ingresso atmosferico e infine una review degli studi condotti in precedenza.
La metodologia seguita viene presentata nel secondo capitolo, nel quale si analizzano i metodi matematici utilizzati nell'analisi aerodinamica e la loro implementazione numerica.
Il terzo capitolo invece riporta i risultati ottenuti. Questi sono divisi in campi istantanei, medi e RMS (valore quadratico medio). Inoltre, oltre allo studio della scia lungo l'asse di simmetria della capsula, attraverso grafici monodimensionali, l'analisi POD (Proper Orthogonal Decomposition) è presentata per analizzare la turbolenza.
Con i risultati ottenuti si vuole valutare il comportamento del flusso attorno alla capsula in questo caso specifico, confrontandone l'andamento con i risultati ottenuti per velocità inferiori. In questo modo si desidera fornire supporto ad ulteriori studi volti a comprendere gli aspetti aerodinamici coinvolti nelle fasi di rientro atmosferico.

Abstract

This work will focus on the atmospheric entry of a capsule, modeled from the ExoMars descent module, into the Martian atmosphere. Since this phase is critical for the success of the mission, the understanding of the aerodynamical phenomena that occur is fundamental. Therefore, the work analyzes the flow behavior around the capsule when the Mach number is 5 at the angle of attack 0°. The obtained results are compared to the Mach 2 case, giving a better understanding of the phenomenon. A Large Eddy Simulation of the compressible flow is performed, obtaining a good representation of the problem. The atmosphere is considered as made only of carbon dioxide (CO_2) with heat capacity $\gamma = 1.33$ and the flow will be analyzed using $Re = 10^6$. The results are analyzed focusing on both the shock wave and the turbulent wake, looking at instantaneous, mean and RMS fields. A Proper Orthogonal Decomposition (POD) analysis is performed to better understand the turbulent region behind the capsule.

Contents

List of Figures

List of Tables

Chapter 1

Introduction

Mars has always held a special fascination status throughout human history. With the beginning of Space exploration in 1957, corresponding to the launch of Sputnik by the Union of Soviet Socialist Republics, a series of missions followed one another, with intent to reach Martian orbit, both from the United States and the U.S.S.R. After years of failed missions, the first mission to orbit Mars was the Mariner 4 in 1964. It took almost ten years and multiple failures before a successful landing took place. In 1971 Mars 3 successfully landed on Mars but the communications were lost after only 20 seconds. In 1975 the Viking 1 lander sent back the first image from the surface and Mars soil was studied for the first time. Once the feasibility of landing on Mars was proven, robotic exploration of the surface began.
Mars exploration is important for many reasons: not only it is the most accessible planet in the solar system, thanks to its proximity but it could also help find answers to the origin and evolution of life [28]. Mars is considered a unique planet, with complex and diverse geology, characterized by a climate that changed through history. Its similarities with Earth makes studying its evolution very interesting: it could lead to uncovering details of Earth and, in general, planetary evolution [5]. Recent discoveries show the possible presence of liquid water on Mars, either in the past or preserved in the subsurface today. Water is the key to life formation so the search for life on Mars's surface increased the interest in the exploration of the Red Planet.
This huge interest in Mars resulted in numerous missions but not all of them were successful. Out of 20 missions, only 11 had a successful landing, as shown in table 1.1.

Mission Name	Agency	Year	Status
Mars 3	Roscosmos	1971	Landing successful but lost communication
Mars 6	Roscosmos	1973	Failure on descent
Mars 7	Roscosmos	1971	Missed planet
Viking 1 and 2	NASA	1975	Success
Phobos 2	Roscomos	1988	Lost communication before entry
Mars 96	Roscomos	1996	Launch vehicle failure
Mars Pathfinder	NASA	1996	Success
Mars Polar	NASA	1999	Landing failed
Beagle 2	ESA	2003	Landing sucessful but communication not working
Mars Exploration Rover (Spirit and Opportunity)	NASA	2003	Success
Phoenix	NASA	2007	Success
Mars Science Laboratory (Curiosity)	NASA	2011	Success
Phobos-Grunt /Yinghuo-1	Roscomos/ CNSA	2011	Launch failure
ExoMars/Schiaparelli	ESA	2016	Landing failed
Mars Insight Lander	NASA	2018	Success
Zhurong Rover	CNSA	2020	Success
Mars 2020 Perseverance Rover	NASA	2020	Success

Table 1.1: List of Mars exploration missions [29]

As shown on the table, not all the lander that reached Mars orbit were able to land. The Entry, Descent and Landing phase (EDL) represents a very critical phase of the mission. It involves phenomena with complex interactions that are not fully clear yet. This phase is divided in three parts: the Entry, which starts at about 200 km of altitude, where the capsule uses the aerodynamic drag to decelerate, the Descent, at around 10 km above the surface, where the parachute is deployed and the Landing.
The objective of this work is the analysis of the behavior of the flow around the ExoMars capsule during the descent at Mach 5 and the comparison with the data obtained for Mach 2 flow.

1.1 ExoMars

The ExoMars program is a collaboration between the European Space Agency (ESA) and Roscosmos, with aim to investigate if life ever existed on Mars while demonstrate new technologies. The program is composed of two missions: the first one, launched in 2016, consists of an orbiter, the Trace Gas Orbiter, and a landing demonstrator module, called Schiaparelli. The second one, featuring the Rosalind Franklin rover, is currently suspended and waiting for a launch date. This mission will enabling technologies relative to surface mobility, sample acquisition and access to the subsurface while analyzing the obtained samples to determine whether or not life on Mars ever existed.

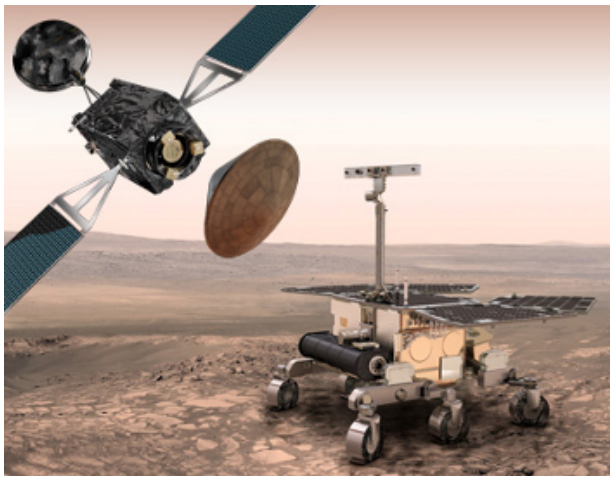

Figure 1.1: Exomars Programme elements. The TGO and Schiaparelli are shown on the left and the Rosalind Franklin rover on the right [1]

The Trace Gas Orbiter main goal is to study atmospheric trace gas to investigate the Martian atmosphere and look for traces of life, by detecting methane, a gas considered an indicator of life. Another task assigned to the orbiter was the release of the Schiaparelli Entry Demonstrator Module (EDM). This spacecraft had the objective of retrieving atmospheric vertical profiles of density, pressure and temperature with higher resolution than remote sensing observation.
On board of the Schiaparelli EDM were mounted different sensors used to register data during the descent. In particular, COMARS (Combined Aerothermal and Radiometer Sensors Instrument Package) and AMELIA (Atmospheric Mars Entry and Landing Investigation and Analysis) were used to analyze the atmosphere during the Entry, Descent and Landing sequence. Obtaining the in-situ measurements allow the creation of atmospheric profiles, which play a significant role in cross calibrations of remotely-sensed observations, testing atmospheric models and resolving practical issues of reaching Mars surface. Only seven profiles were obtained before by in-situ measurements, making the ones of Schiaparelli even more important [15].
The EDLS, Entry, Descent and Landing System plays a crucial role in mission success, hence the need to develop and validate the technologies linked to the environmental and aerodynamic conditions it will face. The measurements obtained during this sequence are used as triggering events of the descent sequence: one malfunction can lead to mission failure, as happened for Schiaparelli. On December 19, 2016, the EDM entered the atmosphere as planned but the signal was lost about 1 minute before the expected touchdown. Investigations showed that during parachute descent the gyros were saturated by unexpected dynamics of the capsule. This resulted in an error in the guidance and control system and a premature release of the parachute, leaving the module free-falling from an altitude of about 3.7 km, reaching an impact speed of 540km/h [2]. Even though the EDM crashed to the ground, the transmitted data during the descent were enough to continue the analysis.

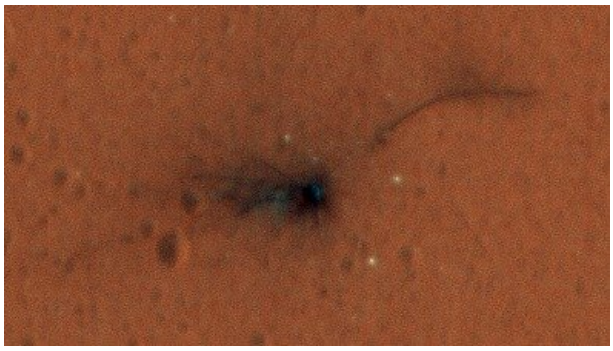

Figure 1.2: Schiaparelli impact site, photographed by NASA's Mars Reconnaissance orbiter [2]. It shows the module, front shield and parachute, still attached to the back-shield. The separation of the sections was successful and the debris are close to the target landing site.

Figure 1.3 shows the overall schematics of the Schiaparelli EDM. The capsule is composed of two parts: the front shield, a 70 ° sphere-cone with a nose diameter of 0.6 m, and the back shell, a truncated cone with 47° inclination. The segment where the two sections meet, has diameter 2.4 mm and contains the Surface Platform, where the lander instruments are mounted.

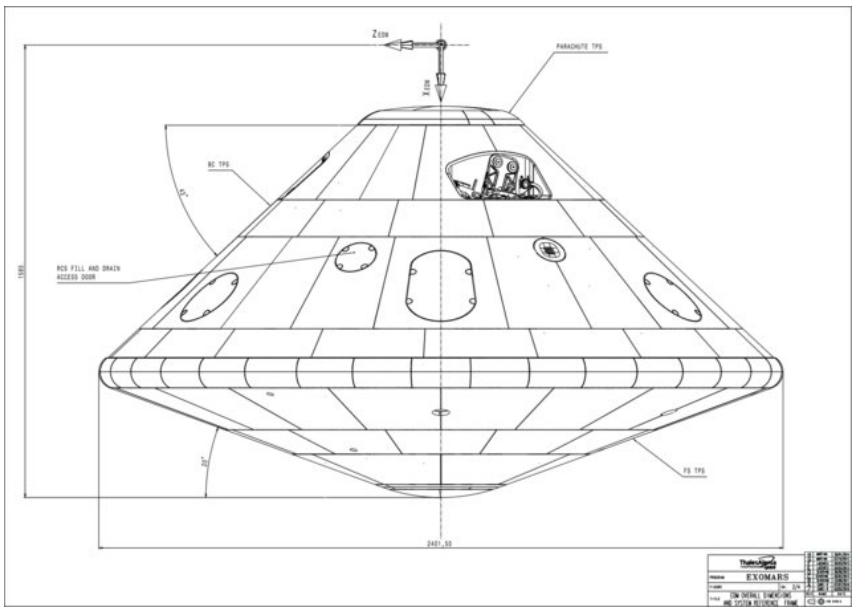

Figure 1.3: Schiaparelli overall schematics [9]

As it will be explained in the next section, the blunt cone configuration has been proved to be the best nose cone shape both in aerodynamic and heat transfer terms.

1.2 Blunt Cone concept and capsule shape

During the Cold War, the search for a more heat-efficient nose shape became one of the centers of aerodynamic studies. Before the launch of Soviet Sputnik 1, which declared the start of the Space Race, the American army, air force and NACA, National Advisory Committee for Aeronautics, were studying a nose shape that could resist the re-entry heat with the aim to

implement it in a warhead. This could be mounted on a missile and used as an intercontinental weapon.
After the end of World War II, the Americans brought Wernher von Braun and his team to the United States, with the intention to develop an intermediate-range ballistic missile program. The idea was to launch a warhead into a suborbital flight which would then re-enter the atmosphere and hit a precise target. This subjected the warhead to high temperatures therefore the needle nose design used in supersonic planes had to be changed. A needle nose shape minimizes the intensity of the shock wave that is formed due to the hypersonic speed, minimizing the atmospheric drag which implies an improvement in efficiency.
In 1953 NACA aerodynamicists H. Julian Allen and Alfred Eggers carried out an analysis of the motion and heating of a re-entering nose cone. [19].Once they calculated the total heat input for different shapes, they obtained that a blunt shape was the one that minimized the total heat input the best. Moreover, they discovered that to minimize the maximum rate of the heat transfer, averaged over the entire vehicle, the nose had to be either very sharp or very blunt. Since the heat-transfer rates were highest at the nose tip and the aim was to minimize it, they concluded that "not only should pointed bodies be avoided, but the rounded nose should have as large a radius as possible".
For atmospheric re-entry, the atmospheric drag is used to slow down the body and an intense shock wave is desired. The kinetic energy in the hypersonic flow is converted into internal energy of the gas across the shock wave and therefore the shock layer near the nose is subjected to high temperatures. This loss of kinetic energy is translated into the deceleration of the body. [8]. As Allen and Eggers found out, the blunt body creates a very strong wave, which produces intense heating. This heat is mostly carried away in the flow and the boundary layer originated serves as an insulator. By contrast, a slender cone produces a shock wave that is less intense and closer to the surface of the nose, as shown in figure 1.4. The boundary layer in this case is too thin to offer protection and the skin friction produces still more heating, for the boundary layer now received energy from the heated air flowing close to the surface.
This theoretical analysis was put to the test on different occasions. The first one, using the X-17, a three-stage missile, aimed to test the maximum Mach reached by different nose cone shapes . In order to do so, an "over the top" mode was preferred to the high ballistic trajectory. This mode consisted of climbing to an altitude of 105 to 160 km, using the first stage and followed by a turnaround and a descent. The system, now pointed downwards, was subjected to a free fall until it reached an altitude of 30,45 km, where the other two stages fired up, accelerating the nose cone to maximum speed. In table 1.2 the maximum values of Mach and the relative altitude of attainment are written for different shapes. These values were obtained during the test flights of the X-17 between July 1956 and March 1957.

Geometry	Maximum Mach	Altitude [km]
Hemisphere	13.7	16,45
Blunt	14.2	17,98
Blunt Cone	14.4	17.37
Cubic Paraboloid	13.8	17.83

Table 1.2: Maximum values of Mach, with relative altitude of attainment, reached during the X-17 flight test [19]. Four different shapes are considered.

An observation can be made by looking at this table: at approximately the same altitude, the blunt cone nose cone reached the higher value of Mach, showing that this shape is the solution that can best withstand the atmospheric entry velocity from low orbit, which is around 8 km/s

or expressed as Mach number, 23. Further tests, conducted using Jupiter and Atlas rockets, reached the maximum speed of 20 Mach, utilizing a long cone with a rounded tip nose cone. When the first Sputnik reached orbit, the main interest of the American aerodynamic research shifted to orbital flight, at first and later to reaching the Moon. Maxime Faget of NACA-Langley, in 1958, calculated thermal loads and heat-transfer rates around different shape. The selected shape was again a cone with rounded tip facing the flow. He then focused his research on the shape of the after body. After numerous tests, he found out that the best solution was a domed after body. This discovery was used for all entry modules, starting with Mercury and Gemini. As shown in figure 1.4, the shape of the back of the capsule influences the behavior of the flow behind it. In fact, where the geometry changes, the boundary layer separates, originating a re-circulation region behind the back shell. This region, characterized by the presence of vortexes, ends in a turbulent wake. At the end of the entry sequence, as it will be explained later in this work, a parachute is used to slow down the capsule. The turbulent wake represents a problem for the parachute since this flow is affected by instabilities. Using a cone or dome shape in the back-shell allow to reduce the width of this region by reducing the thickness of the detached boundary layer.

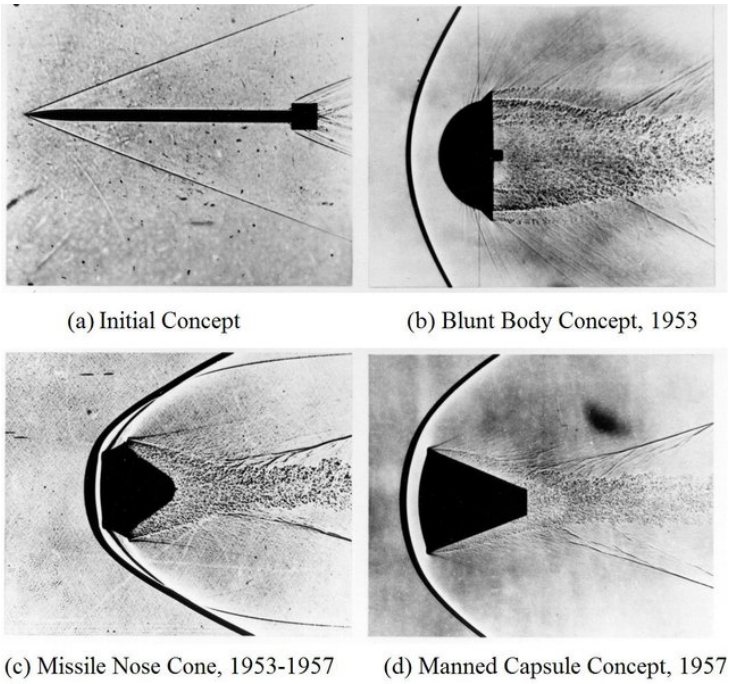

Figure 1.4: Shadowgraph images that represent early vehicle reentry concepts [31]. Here the difference between slender and blunt cone is clear. A comparison is also made for the blunt angle shape used in the missile nose cones and in the blunted cone used for manned capsule.

1.3 Entry, Descent and Landing phase

The Entry, Descent and Landing is the most critical phase of the mission: other than being responsible of the successful landing of the lander, its trajectory and variations define the final landing site. Due to the impossibility of sending commands to the entry capsule when the final phase of the flight begins, both the landing site and the entire EDL sequence are pre-defined. In particular, the landing site is defined as a large ellipse where the lander can land without

compromising the mission. For Schiaparelli, the landing site, figure 1.5, measured 100 km by 15 km.

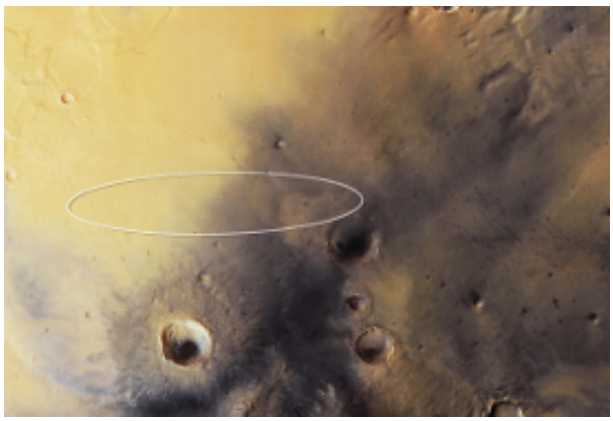

Figure 1.5: ExoMars Schiaparelli landing ellipse [3]

The uncertainties in the descent trajectory due to the variations in atmospheric density, turbulence and wind speed are one of the problems that the capsule can come across. The other problems are originated from the impossibility of commanding the capsule during the sequence. As happened in the Schiaparelli case, for example, anomalies detected by the sensors can be fatal for the mission.
In figure 1.6, is shown the programmed sequence for Schiaparelli. The EDL starts when the capsule, released from the TGO a few days before, reaches the atmosphere at a Mach number of 25, 121 km from the surface. The whole sequence is 6 minutes long and is divided into three parts. The first one, the Entry, consists in a 3-minute long, high-speed ballistic entry into the atmosphere. During this, the capsule is subjected to high temperatures due to the formation of the shock way. The kinetic energy is dissipated, slowing down the capsule which, at the end of the entry phase is moving at Mach 1,3. At the end of this phase, which corresponds to an altitude of 10 km, the parachute is opened and the Descent phase starts. The capsule reaches the subsonic regime thanks to the passive action of the parachute and loses the heat shield, not necessary anymore. The following and last part is the Landing phase. The approach followed depends on the size and complexity of the lander [4].

- Small spacecrafts, such as Mars Pathfinder, use a descent system that involves a 20 m long cable to lower the lander. Right before touchdown airbags inflate forming a ball around the lander. This protects the lander once the cable is cut and the solid rockets, used to slow down the descent, are turned off, dissipating the remaining velocity bouncing on the surface of Mars;

- For the most recent landers, which are also the heavier rovers yet built, a new sky crane has been developed. The spacecraft can steer itself during atmospheric entry and uses both a parachute and retrorockets to slow down. In the final seconds of the landing, the upper stage lowers the rover on a tether to land it on its wheels.

- For Schiaparelli, and other middle-sized landers, the procedure is the same adopted for Viking 1. This consists of an active proximity phase where retrorockets are fired to slow down, ensuring a final horizontal position at touchdown. A short free fall to the surface occurs after the engine is cut out.

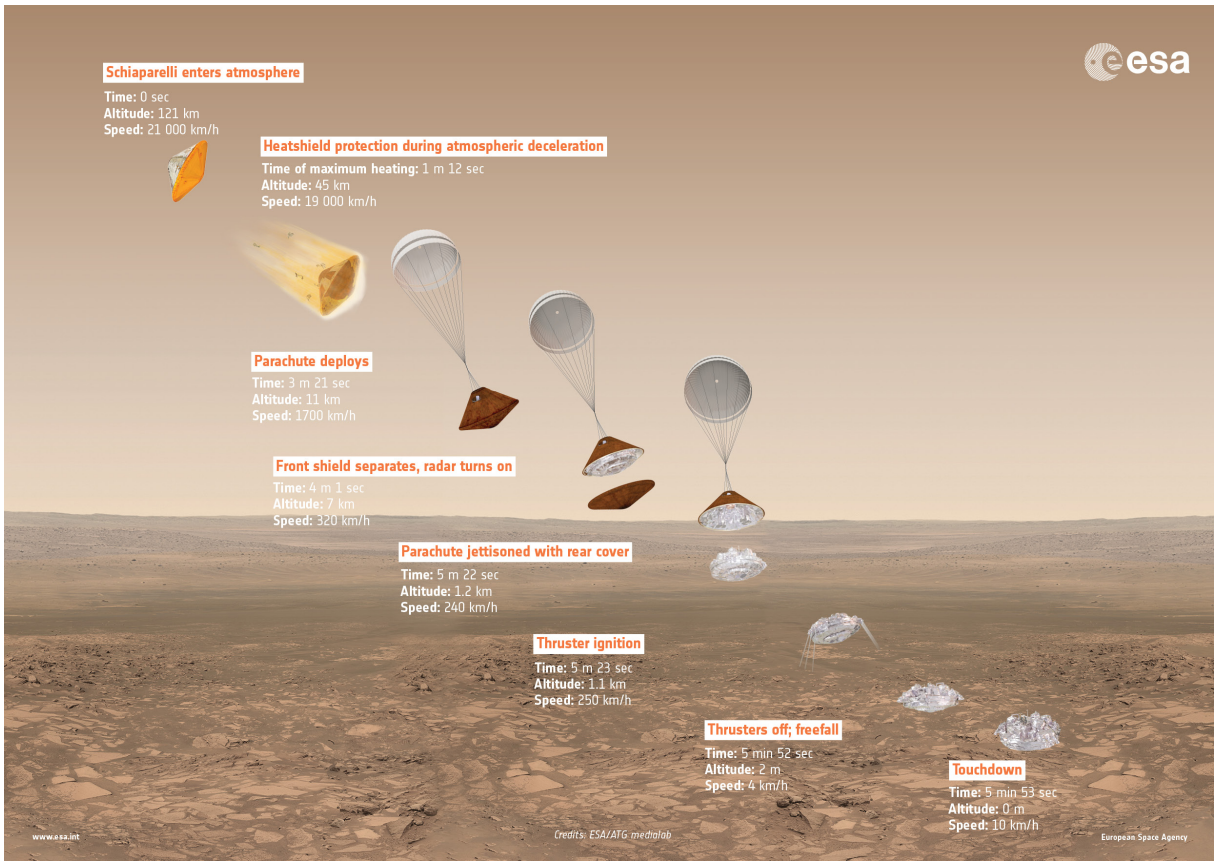

Figure 1.6: ExoMars Entry,Descent and Landing sequence [3]. For each event are highlighted the time, altitude and speed at which they occur.

1.4 Literature Review

Aerothermodynamics of entry vehicles has been studied with both experimental and computational studies, over the past 60 years. Experimental studies of blunt body hypersonics started with the Mercury and Apollo programs while the computational was implemented beginning with the Apollo and Space Shuttle programs. Brian R. Holli in his book "Experimental and Computational Aerothermodynamics of a Mars Entry Vehicle" [20] presents a quick history of studies of hypersonic flows around a 70° sphere-cone geometry. Although this book was written in 1996, regarding the Mars Pathfinder Mission, the experimental and computational methods that are here illustrated are still used today, since the shape of the capsule is almost unchanged (figure 1.7).

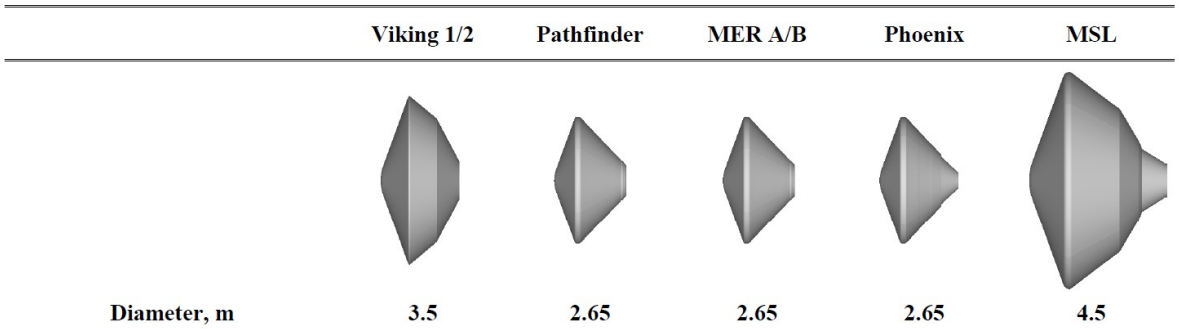

Figure 1.7: Comparison of Mars entry vehicle dimensions, starting with the Viking 1 and 2. The other are the entry vehicle used to land the rover Spirit and Opportunity (MER A/B), the lander Phoenix and Curiosity Rover (MSL) [14]. This are the successful missions that landed on Mars before ExoMars

Starting with the experimental approach, the earliest documented heat-transfer data on large-angle conical bodies are from Stewart and Marvin, in 1969 citemarvin1969convective. They tested sphere cone models with a half angle of 50° to 70° in the NASA Ames 42-Inch Shock Tunnel in air at M=15, changing the angle of attack from 0° to 30°. In particular, they found that the zero-degree angle of attack agreed well with the analytical solution. In 1992 Shimshi tested 50°, 60° and 70° sphere-cone models at NASA LaRC 15-inch Mach 10 Air Tunnel with Reynolds number of 1 to 4×10^6 and angle of attack from 0° to 20°. [32]. The results showed an expected decrease in the heating of the stagnation point and an increase in corner heating, with increasing cone angle. These observations are a consequence of the increasing cone angle because it implies an increase in the nose radius and the movement of the sonic line along the cone to the corner. Shimshi used also an inviscid code to provide edge conditions for boundary layer computations. He obtained good agreement with exceptions of small discontinuities in predictions around the stagnation region.
While most of the experiments were done in air environments, Stewart and Chen in 1993, tested 70° sphere-cones with different corner radii in CO_2 and CO_2-Ar environments, with 0°, 10° and 20° angle of attack. [33]. They also computed Navier-Stokes solutions for the 0° case, using a modified version of the NEQ2D code, a 2D axisymmetric nonequilibrium solver. Their results showed qualitative agreement between experiment and computations but magnitudes of heating rates differed from 5% to 45%.
Further studies focused on the 70° sphere cone and the behavior of a low-density flow around it, testing it in air and comparing the results with computational Navier-Stokes solutions and DSMC. The Direct Simulation Monte Carlo (DSMC), code is used to compute the low-density hypersonic flow, which dynamics is poorly approximated by the Navier-Stokes equations. This was proved during the experiments: when the flow was idealized as low-density, Navier-Stokes's solutions differed from the results.
Another interesting experimental study is the one done by Horvath, McGrinnley and Hannemann [22]. They tested a 70° sphere-cone in a flow with Reynolds number ranging from 1×10^6 to 8×10^6 in order to observe the nature of the wake flow field. They observed that it was either transitional or turbulent across the entire range. In terms of computational studies, different approaches have been followed. Other than the Navier-Stokes, NEQ2D and DSMC codes, in 1990, inviscid Euler codes were coupled to axisymmetric analog boundary layer codes to study both perfect gases and non-equilibrium chemistry and radiation effects. For the Pathfinder capsule, a viscous shock layer analysis of the flow around the capsule was carried out by Gupta and Lee [17] in 1993. They saw that non-equilibrium chemistry models were not found to be

significant on the forebody nor was the radiative heat transfer.
During the Pathfinder design, other codes were used, such as the LAURA (Langley Aerothermodynamic Upwind Relaxation Algorithm) and GASP (General Aerodynamic Simulation Program). The first one, used also for the Mars Science Laboratory [14] and Exomars post-flight analysis[12], was used by Mitchletree and others in multiple studies, in 1994, to generate aerodynamic and aerothermodynamics data, analyzing the afterbody and its near wake [26, 25]. They found out that the heating rates were at least one order of magnitude lower in the afterbody than in the forebody and the local maximum was on its base corner. they also identified a large separated recirculation region right after the body. GASP was used one year later by Haas and Venkatapathy to compute forebody and wake solutions, employing a third-order upwind inviscid flux and a finite rate Martian atmospheric chemistry model [18]. Their forebody results were in good agreement with the one obtained with LAURA while the wake flow field results identified the extreme sensitivity of the recirculating region at the base of the vehicle to the grid resolution.
In 2007, the Mars Science Laboratory was characterized using the same computational methods used by the previous missions but the prediction of turbulent transition in the early phase has not been done before. LAURA was used to estimate when the boundary layer transition occurs on the surface, knowing that the transition increases with the increase of the Reynolds number. A comparison between the experimental results showed that, in general, the computational tools unpracticed the perfect gas turbulent data by 15% and that, unlike the past missions, the larger ballistic coefficient and diameter lead to turbulent heating early in the entry trajectory.
Despite numerous studies carried out so far, the dynamic of the entry phase is not yet fully known. The phenomena that occur during this phase are not fully clear yet, therefore more detailed analyses are needed. The objective of this work is the aerodynamical analysis of the flow around the ExoMars capsule in supersonic regime with angle of attack 0°. Using the the in-house solver STREAmS [10], a Large Eddy Simulations (LES) of the compressible flow field that develops around the capsule will be performed, when Mach number is 5. Focusing in the bow shock region, a comparison is made between the results obtained by simulations at Mach numbers 5 and 2. One-dimensional study along the capsule symmetry axis and POD analysis will be performed in order to study the turbulent wake.

Chapter 2

Methodology

In this chapter the methodology followed in the current fluid dynamical analysis is discussed in terms of mathematical and numerical approach, along with fluid-structure interface modeling.

2.1 Mathematical Approach

Navier-Stokes equations are used to describe the flow, remaining in the continuum mechanic hypothesis (the mean distance traveled by a molecule between collisions with other molecules is smaller than the length of the fluid systems).
While the capsule moves through the hypersonic flow, a detached bow shock is formed in front of it. Using the Shock Expansion Theory it is possible to analyze the shock wave as a coexistence of normal and oblique shocks.
The shock wave is used to decelerate the vehicle, transforming the kinetic energy in heat. This heat can excite the vibrational internal energy of the molecules of the gas, inducing dissociation and ionization. This forces a change in the model used to idealize gases from calorically to thermally perfect.
Behind the capsule, a turbulent region is formed. This is characterized using the energy cascade model and Kolmogorov hypothesis.

2.1.1 Navier-Stokes Equations

Navier-Stokes equations (2.1.1) are used to describe the flow, idealized as a compressible ideal gas. The following system of equations describes the mass, momentum and energy conservation.

$$\begin{cases} \dfrac{\partial \rho}{\partial t} + \dfrac{\partial (\rho u_j)}{\partial x_j} = 0 \\ \dfrac{\partial (\rho u_i)}{\partial t} + \dfrac{\partial (\rho u_i u_j)}{\partial x_j} + \dfrac{\partial p}{\partial x_i} - \dfrac{\partial \sigma_{ij}}{\partial x_j} = 0 \\ \dfrac{\partial (\rho e)}{\partial t} + \dfrac{\partial (\rho e u_j + p u_i)}{\partial x_j} + \dfrac{\partial q_i}{\partial x_i} - \dfrac{\partial (\sigma_{ij} u_i)}{\partial x_j} = 0 \end{cases} \tag{2.1.1}$$

where ρ is the density, u_i, u_j are the components of the velocity respectively in the i-th and j-th direction, p the thermodynamic pressure, obtained as the product of density, specific gas constant R and temperature T, while e is the total energy per unity of mass, expressed as:

$$e = c_v T + \frac{u_i u_i}{2} \tag{2.1.2}$$

with c_v the specific heat at constant volume. The remaining quantities are the total heat flux

$$q = -\lambda \left(\frac{\partial T}{\partial x_i} \right) \tag{2.1.3}$$

with λ the heat transfer coefficient and, finally, the viscous stress tensor

$$\sigma_{ij} = \mu \left(\frac{\partial u_i}{\partial x_j} + \frac{\partial u_j}{\partial x_i} - \frac{2}{3} \frac{\partial (u_k)}{\partial x_k} \delta_{ij} \right) \tag{2.1.4}$$

where μ is the dynamic viscosity of the gas.
In order to reduce the computational cost, the Navier-Stokes equations need to be expressed in a non-dimensional formulations. The number of independent parameters is reduced from 15 to 4, using the following relationships:

$$\begin{cases} R_0 = \dfrac{p_0}{\rho_0 T_0} \\ u_0 = \sqrt{R_0 T_0} \\ t_0 = \dfrac{l_0}{u_0} \\ \mu_0 = \rho_0 u_0 l_0 \\ \lambda_0 = \mu_0 R_0 \\ c_{p0} = \dfrac{\gamma}{\gamma - 1} R_0 \\ c_{v0} = \dfrac{R_0}{\gamma - 1} \\ e_0 = c_{v0} T_0 + \dfrac{u_0^2}{2} \end{cases} \tag{2.1.5}$$

Here the reference values are ρ_0, p_0, T_0, l_0, which correspond to the density ρ_∞, pressure P_∞ and temperature T_∞ of the upstream flow and the capsule maximum diameter. c_{p0} and γ are respectively the specific heat at constant pressure and the ratio of specific heats.
Now, dividing the dimensional values by the reference values, the non-dimensional quantities are obtained: $\rho' = \rho/\rho_0$, $p' = p/p_0$,$T' = T/T_0$,$x' = x/l_0$,etc.
The use of non-dimensional quantities is convenient because the free-stream ones become unitary ($\rho'_\infty = p'_\infty = T'_\infty = R'_\infty = 1$) while it is possible to define the following non-dimensional groups:

- free-stream Mach $\rightarrow M_\infty = \dfrac{u_\infty}{\sqrt{\gamma R_0 T_0}}$
- Reynolds number $\rightarrow Re = \dfrac{\rho_0 u_\infty l_0}{\mu_0}$
- Prandtl number $\rightarrow Pr = c_{p0} \dfrac{\mu_\infty}{\lambda_\infty}$

Once all these values are known, the free-steam quantities can be calculated as

$$u'_\infty = \frac{u_\infty}{u_0} = \frac{M_\infty \sqrt{\gamma R_0 T_0}}{\sqrt{R_0 T_0}} = \sqrt{\gamma} M_\infty \tag{2.1.6}$$

$$\mu'_\infty = \frac{\mu_\infty}{\mu_0} = \frac{\rho_0 u_\infty l_0}{Re} \frac{1}{\rho_0 u_0 l_0} = \frac{\sqrt{\gamma} M_\infty}{Re} \tag{2.1.7}$$

$$\lambda'_\infty = \frac{\lambda_\infty}{\lambda_0} = \mu_\infty \frac{c_{p0}}{Pr} \frac{1}{\rho_0 u_0 l_0 R_0} = \frac{\gamma}{\gamma - 1} \frac{1}{Pr} \frac{\sqrt{\gamma} M_\infty}{Re} \tag{2.1.8}$$

Substituting the non-dimensional quantities in the system 2.1.1, omitting the superscript for the sake of clarity, the Navier-Stokes equations become:

$$\begin{cases} \dfrac{\partial \rho}{\partial t} + \dfrac{\partial(\rho u_j)}{\partial x_j} = 0 \\ \dfrac{\partial(\rho u_i)}{\partial t} + \dfrac{\partial(\rho u_i u_j)}{\partial x_j} + \dfrac{\partial p}{\partial x_i} - \dfrac{\sqrt{\gamma} M_\infty}{Re} \dfrac{\partial \sigma_{ij}}{\partial x_j} = 0 \\ \dfrac{\partial(\rho e)}{\partial t} + \dfrac{\partial(\rho e u_j + p u_i)}{\partial x_j} - \dfrac{\sqrt{\gamma} M_\infty}{Re} \left[\dfrac{\gamma}{\gamma - 1} \dfrac{1}{Pr} \dfrac{\partial q_i}{\partial x_i} + \dfrac{\partial(\sigma_{ij} u_i)}{\partial x_j} \right] = 0 \end{cases} \tag{2.1.9}$$

2.1.2 Shock Expansion Theory

As already stated in the previous lines, the shock that is originated from an hypersonic flow around a blunt object is a curved bow shock. This is one instance where all possible oblique shocks can be observed at once for a given value of Mach.
The Shock Expansion Theory is the combination of oblique-shock relations and Prandtl-Meyer wave relations. It is used to determine the flow properties and forces for simple 2-D shapes in supersonic flow.
Let's consider a body with deflection angle θ, invested by a supersonic flow with upstream velocity V_1 and Mach number $M_1 = V_1/a_\infty > 1$. The angle between the originated shock wave and the flow direction is called wave angle and it is indicated as β (figure 2.1). This angle can assume values between 90° and $\mu = sin^{-1}(\dfrac{1}{M_1})$, wave angle of the Mach wave, line of disturbances obtained when the propagation velocity of the wave is the same as the sound velocity.

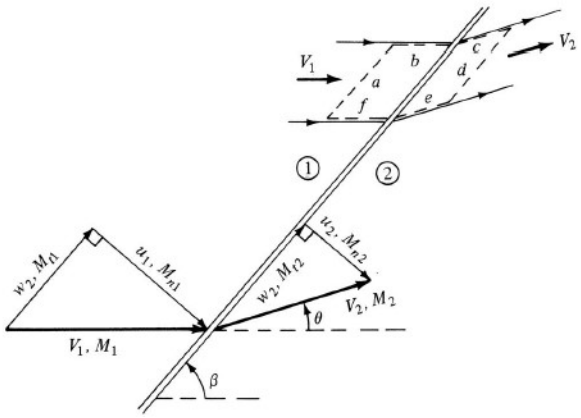

Figure 2.1: Schematics of an oblique shock. In the higher part is shown the control volume used in the calculations.[7]

Indicating with subscript 2 the downstream quantities, the relationships between the flow before and after the shock are obtained applying the Navier-Stokes equations to the control volume, delimited by dashed lines in the upper part of figure 2.1. Defined the normal component of the upstream Mach as

$$M_n = M sin\beta \tag{2.1.10}$$

the oblique shock relations are the following

$$M_{n,2}^2 = \frac{1 + [(\gamma - 1)/2] M_{n,1}^2}{\gamma M_{n,1}^2 - (\gamma - 1)/2} \tag{2.1.11}$$

$$M_2 = \frac{M_{n,2}}{sin(\beta - \theta)} \tag{2.1.12}$$

$$\frac{\rho_2}{\rho_1} = \frac{(\gamma+1)M_{n,1}^2}{2+(\gamma-1)M_{n,1}^2} \tag{2.1.13}$$

$$\frac{p_2}{p_1} = 1 + \frac{2\gamma}{\gamma+1}(M_{n,1}^2 - 1) \tag{2.1.14}$$

$$\frac{T_2}{T_1} = \frac{p_2}{p_1}\frac{\rho_1}{\rho_2} = \left[1 + \frac{2\gamma}{\gamma+1}(M_{n,1}^2 - 1)\right]\left[\frac{(\gamma+1)M_{n,1}^2}{2+(\gamma-1)M_{n,1}^2}\right] \tag{2.1.15}$$

These equations state that the oblique shock wave properties are dependent only on the upstream M_n, considering a calorically perfect gas. The properties of this gas are described in the next section.
From equation 2.1.10, the normal Mach depends on both M_1 and β. It follows that a normal shock is a particular type of oblique shock, where $\beta = 90$. In this case, the Mach normal M_n in equations 2.1.13,2.1.14,2.1.15 is replaced by M_1 $(sin(90) = 1)$
Equations 2.1.12 shows that in order to obtain the Mach number after the shock, both θ and β are needed. An equation, called the $\theta - \beta-$M relation, can be obtained from the ratio of the normal velocities u_1, u_2. Writing

$$tan\beta = \frac{u_1}{w_1} \qquad\qquad tan(\beta - \theta) = \frac{u_2}{w_2} \tag{2.1.16}$$

and knowing that the tangential component w does not change, the $\theta - \beta-$M relation 2.1.17 is obtained from the equation

$$\frac{u_1}{u_2} = \frac{tan\beta}{tan(\beta-\theta)} = \frac{(\gamma+1)M_1^2 sin^2\beta}{2+(\gamma-1)M_1^2 sin^2\beta}$$

$$tan\theta = 2\cot\beta \frac{M_1^2 sin^2\beta - 1}{M_1^2(\gamma + cos2\beta) + 2} \tag{2.1.17}$$

This equation defines a maximum value of θ above which there is no solution. Such angle represents the maximum inclination the body can have for the oblique shock to occur. Higher values of θ produce detached shock waves.
Another observation that can be made from the $\theta-\beta-$M relation is that for each combination of θ and M the equation gives two values of β. These represent different intensities of oblique shock wave: the higher value describes a strong shock, where the flow downstream is always subsonic, while the weak shock is present when β is smaller and the flow after the wave is supersonic.

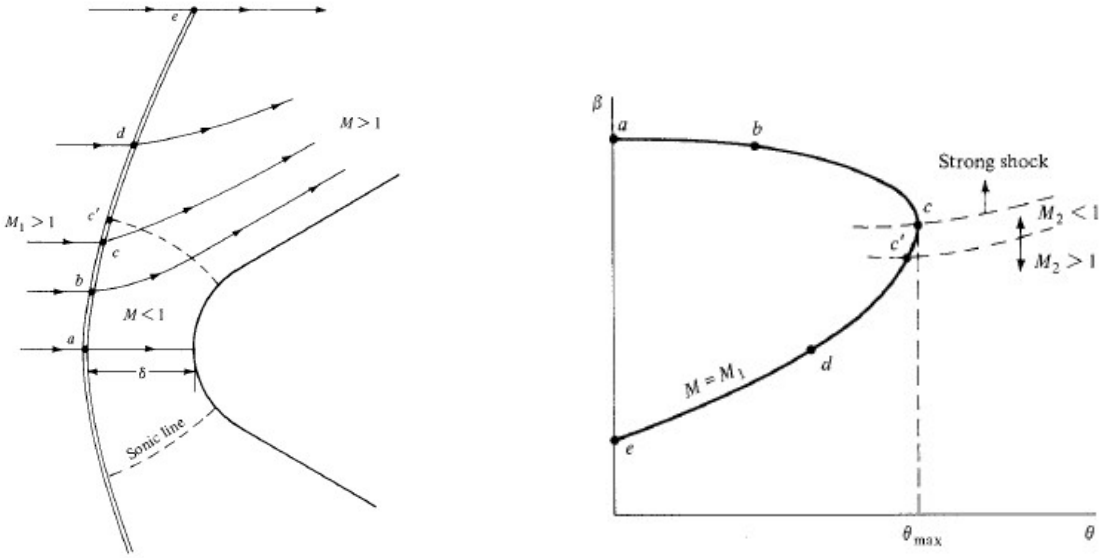

(a) Flow over a supersonic blunt cone

(b) $\theta - \beta - M$ diagram

Figure 2.2: Sketch of the supersonic flow around a blunt cone and its $\theta - \beta - M$ diagram [7]

As already stated at the begin of this section, a detached shock wave is a combination of all the oblique shock solutions for a given value of upstream Mach. Figure 2.2 shows the sketch of a shock wave around a blunt cone and the relative $\theta - \beta -$M diagram. In particular, the letters indicate certain values of β, used to describe the different types of shocks that occur.

a : the shock wave is normal to the upstream flow so here the wave is considered as a normal shock wave;

b : the flow is deflected slightly after the wave and it is subsonic. All the points between a and c are strong oblique shocks and the value of β decreases;

c : corresponds to the point where θ_{max} is reached. Here the flow is deflected the maximum;

c' : the flow after the shock becomes sonic creating the sonic line. This line divides the subsonic flow from the supersonic flow that characterizes the downstream flow, between point c' and e;

d : the shock wave is a weak oblique shock. The deviation of the flow is decreasing and the flow remains supersonic.

e : the shock is considered as Mach wave

Therefore the Shock Expansion Theory can describe the changes in pressure, density, temperature and velocity due to the detached shock wave using the equations here presented, changing the value of β.

2.1.3 Calorically and thermally perfect gas

In gas dynamics, gases are divided as perfect or real gases. While real gases are defined as gases where intermolecular forces affect the macroscopic thermodynamic properties, in perfect gases this forces are neglected.

Perfect gases include three categories : calorically, thermally perfect gases and chemically reacting mixture of prefect gases [8]. In this work the gas is considered as pure and chemically non reacting therefore only the calorically and thermally perfect gases are analyzed.
In thermodynamics, the quantities that are used to describe the system are

- pressure P
- specific volume (volume per unit of mass) ν
- density ρ
- temperature T
- internal energy e
- enthalpy h
- entropy S

The internal energy is a microscopic representation of the sum of the energies of the molecules of the material and is used to define the enthalpy as the sum of internal energy and the product of pressure and volume.
Once the specific heats are defined as the amount of heat that must be added to one unit of mass of the substance in order to cause an increase of one unit in temperature, for constant pressure (C_p) or volume (C_v), the differential changes in internal energy and enthalpy of a perfect gas, are written as

$$de = C_v(T)dT \tag{2.1.18}$$

$$dh = C_p(T)dT \tag{2.1.19}$$

These two equations are used for thermally perfect gases, where the specific heats are considered variables and specifically, functions of the temperature. In calorically perfect gases the specific heat are constants and are unique of the gas. In this case the equations are considered in their finite form:

$$e = C_vT \tag{2.1.20}$$

$$h = C_pT \tag{2.1.21}$$

The distinction between the two types of perfect gases is necessary because, as happens in the atmospheric entry, the excitation of vibrational energy within the molecules of the gas and the electronic energy associated with electron motion change the nature of the gas therefore an analysis with calorically perfect gases could be wrong. However, the assumption of calorically perfect gas is made for hypersonic flows when the changes with temperature are negligible.
With exception of entropy, defined as $ds = C_pdT/T - RdP/P$, the other quantities are not affected by the distinction between the two categories. Looking at equation 2.1.22, where the perfect-gas equation of state is written, the quantities shown are not dependent on the specific heat: R is the specific gas constant and depends on the gas itself while pressure, specific volume and temperature are relative to the system.

$$P\nu = RT \tag{2.1.22}$$

2.1.4 Turbulence characterization

The turbulence present in the afterbody of the capsule is characterized by the multiscale mechanism, theorized by Richardson to describe the energy dissipation in turbulence [30].
Turbulence can be considered as a combination of eddies, turbulent motion moderately coherent over a region of size ℓ. Eddies have different sizes and their velocity and timescale are function of their dimension. The energy cascade process, in which energy is transferred between the different sized eddies, is summarized by Richardson thus: "Big whorls have little whorls which feed on their velocity; and little whorls have lesser whorls, and so on to viscosity."
Defined the flow scale as L, the larger eddies are characterized by lenghtscale ℓ_0 compatible to L, velocity u_{ℓ_0} on the order of the root meas square turbulent intensity $u' = \sqrt{\frac{2k}{3}}$, where k is the turbulent kinetic energy. Eddies with dimension smaller than ℓ_0 are characterized by the Kolmogorov hypothesis:

(i) *Local isotropy: at sufficient high Reynolds number, the small-scale turbulent motions($\ell << \ell_0$) are statically isotropic.*

This means that their properties are not varying according to the direction. The value of ℓ where the change between anisotropic and isotripc happens is indicated as ℓ_{EI}[1].

(ii) *First similarity hypothesis: In every turbulent flow at sufficiently high Reynolds number, the statistics of the small-scale motions ($\ell < \ell_{EI}$) have a universal form that is uniquely determined by ν and ε.*

With ν is indicated the kinematic viscosity and ε the dissipation rate. This hypotesis implies that in the range $\ell < \ell_{EI}$, the timescales $\ell/u(\ell)$ are small compared with ℓ/u_{ℓ_0}, so that the small eddies can adapt quickly to maintain a dynamic equilibrium with the energy-transfer rate posed by the large eddies.

(iii) *Second similarity hypothesis: In every turbulent flow at sufficiently high Reynolds number, the statistics of the motions of scale ℓ in the range $\ell_0 >> \ell >> \eta$ have a universal form that is uniquely determined by ε, independent of ν.*

$\eta = (\nu^3/\varepsilon)^{1/4}$ is the lenght of the Kolmogorov scale, the smallest dissipative eddy. Defining the lengthscale ℓ_{DI} [2], where the viscous effects start, the universal equilibrium range is divided in two. The range in the hypothesis becomes $\ell_{EI} > \ell > \ell_{DI}$, called inertial subrange, where motions are determined by inertial effects. In the second range, $\ell < \ell_{DI}$, called dissipation range, the motion experiences significant viscous effects and the dissipation happens here.

[1] interface between the Energy-containing range and Inertial subrange. figure 2.3
[2] interface between the Dissipation range and Inertial subrange. figure 2.3

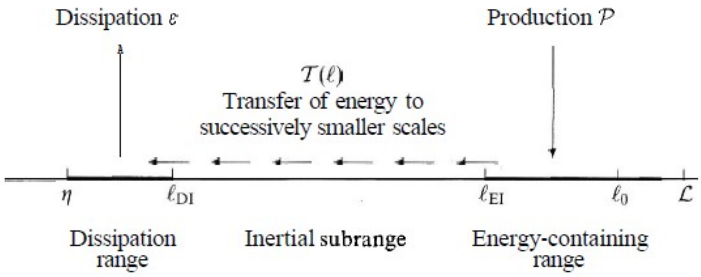

Figure 2.3: Diagram of the energy cascade in a turbulent flow. $\mathcal{P}$ labels the energy that enters the turbulence and is called production while with ε is indicated the dissipated energy. [30]

2.2 Numerical Approach

Numerical simulations allow to predict and simulate the behavior of a system too complex to be analyzed with an analytical approach, such as compressible and incompressible flows. Computational Fluid Dynamics (CFD) is used in this work to evaluate the behavior and properties of the supersonic wake produced by an entry vehicle, utilizing numerical methods to simulate the flow.
Different methods exist to simulate the flow around the capsule. Considered in descending order of computational load, these are:

- Direct Numerical Simulation (DNS): consists in the resolution of Navier-Stokes equation without employing any turbulence closure. It allows to obtain the most accurate reproduction of the flow but it requires the maximum computational load. The result is equivalent to a physical experiment with the same conditions. The system is discretized in both spatial and temporal domain. The dimensions of the discretization must be fine enough to capture the dynamics of the smallest vortical structure while the whole domain and simulation time must be large enough to capture the dynamics of the largest eddies.

- Large-Eddy-Simulation (LES): only resolve large vortical structures. The statistics of the largest scales are dependent on the geometry of the fluid system while the statistics of the small scales are universal. Thus, large-eddy simulations allow simultaneously to treat high Reynolds number flows and to obtain a precise reproduction of turbulence.

- Reynolds Averaged Navier-Stokes (RANS), only resolve the mean flow while all the turbulent scales are treated with an a priori model. It is based on the Reynolds decomposition of the flow field variables and it needs experimental validations.

In this work the method implemented in the analysis of the turbulence is the LES. Three conceptual steps form the entire method.
The first one consists in the definition of the filter, used to divide the resolved part, denoted by ($\bar{}$), to the fluctuating part, labeled with ('). In this case is chosen an implicit filter therefore the grid acts as a filter itself: defined the grid step as $\Delta = \sqrt[3]{\Delta x \Delta y \Delta z}$, the code solves only the turbulence scale bigger than Δ, directly on the grid. When the compressible flow is considered, the flow variables are expressed in terms of Favre variables: called x a generic variable, this is decomposed in a density-weighted part $\tilde{x} = \overline{\rho x}/\overline{\rho}$ and an unresolved part, denoted by ("). Defined the filtering as equation 2.2.1, where the filter G_Δ is applied to the velocity, the second step of this method consists in filtering the Navier-Stokes equations. The filtered Navier-Stokes system of equations is shown in equation 2.2.2.

The third and last step of the LES method is the solving of the filtered Navier-Stokes equations, obtaining the simulation of the large eddies in the turbulent flow.

$$\tilde{u_i}(x,t) = \int G_\Delta(r,x) u_i(\overrightarrow{x} - \overrightarrow{r}, t) dr \tag{2.2.1}$$

$$\begin{cases} \dfrac{\partial \bar{\rho}}{\partial t} + \dfrac{\partial(\bar{\rho}\tilde{u_j})}{\partial x_j} = 0 \\ \dfrac{\partial(\bar{\rho}\tilde{u_i})}{\partial t} + \dfrac{\partial(\bar{\rho}\tilde{u_i}\tilde{u_j})}{\partial x_j} + \dfrac{\partial \bar{p}}{\partial x_i} + \dfrac{\sqrt{\gamma}M_\infty}{Re}\dfrac{\partial \overline{\sigma_{ij}}}{\partial x_j} + \dfrac{\partial \overline{\tau_{ij}}^{SG}}{\partial x_j} = 0 \\ \dfrac{\partial(\bar{\rho}\tilde{e})}{\partial t} + \dfrac{\partial(\bar{\rho}\tilde{e}\tilde{u_j} + \tilde{p}\tilde{u_j})}{\partial x_i} - \dfrac{\sqrt{\gamma}M_\infty}{Re}\left[\dfrac{\gamma}{\gamma-1}\dfrac{1}{Pr}\dfrac{\partial \tilde{q_i}}{\partial x_j} + \dfrac{\partial(\overline{\sigma_{ij}}\tilde{u_i})}{\partial x_j}\right] + \dfrac{\partial \overline{e_j}^{SG}}{\partial x_j} = 0 \end{cases} \tag{2.2.2}$$

where

$$\overline{\tau_{ij}}^{SG} = \bar{\rho}(\overline{u_i u_j} - \tilde{u_i}\tilde{u_j}) \qquad \overline{e_j}^{SG} = \overline{\rho e u_i + p u_i} - (\bar{\rho}\tilde{e_T}\tilde{u_i} + \bar{p}\tilde{u_i}) \tag{2.2.3}$$

The terms in 2.2.3 are respectively the sub-grid stress tensor and energy and represents the unresolved turbulence contributions due to the filtering process. These contributions can be treated using two different techniques. The first one is called explicit LES and the residual terms are treated with an a priori model. The second one, employed in this work, is the implicit LES and the effects of the residual term are emulated by the intrinsic numeric dissipation. In fact, the numerical discretization of Navier-Stokes equations with finite-difference methods generates an artificial dissipation, whose effect is somehow similar to that of the eddy viscosity. Employing the implicit LES, the code used can solve the Navier Stokes equations 2.1.1 without adding any external model. In the particular case of this work, the solver used is STREAmS, developed by the research group at the Sapienza University of Rome [10].
STREAmS (Supersonic TuRbulent Accelerated navier-stokes Solver) is an "high-fidelity solver for DNS of compressible wall-bounded flows": by implementation of the Immersed Boundary Method, is able to simulate the flow around complex geometries, such as the ExoMars capsule, and the originated wake behind it.
Starting from equations 2.1.1, the convective terms are discretized using a hybrid energy-preserving/ shock-capturing scheme. Considering the convective flux in the x direction, for example, $f_x = \rho u \phi$, where ϕ is the transported quantity ($\phi = 1$ for the mass equation, $\phi = u_j$ in the momentum equation and $\phi = h$, total enthalpy, for the energy equation), the numerical discretization of the stream-wise derivative of the flux, expressed at the i-th node, is:

$$\left.\frac{\partial f_x}{\partial x}\right|_i = \frac{1}{\Delta x}(\hat{f}_{x,i+1/2} - \hat{f}_{x,i-1/2}) \tag{2.2.4}$$

where Δx is the spacing of the mesh. Defined the three-point averaging operato as:

$$\widetilde{(F,G,J)}_{i,l} = \frac{1}{8}(F_i + F_{i+l})(G_i + G_{i+l})(J_i + J_{i+l}) \tag{2.2.5}$$

the numeric flux at the interface $i + 1/2$ is obtained by recasting in conservative form the split formulation of the Eulerian fluxes

$$\hat{f}_{x,i+1/2} = 1\sum_{l=1}^{L} a_l \sum_{m=0}^{l-1} \widetilde{(\rho, u, \phi)}_{i-ml} \tag{2.2.6}$$

where a_l are the standard coefficients for central finite-difference approximations of the first derivative of order 2L. In smooth, shock free regions, an energy-consistent flux is applied, ensuring that the total kinetic energy is discretely preserved in the case of inviscid incompressible

flow. This locally conservative formulation allows straightforward hybridization of the central flux with classical shock-capturing reconstructions. In the case at hand, shock capturing capabilities rely on the use of the Lax-Friedrichs flux vector splitting: the the components of the positive and negative characteristic fluxes are reconstructed at the interfaces using Weighted Essentially Non-Oscillatory (WENO) scheme. A modified version of the Ducros shock sensor (eq 2.2.7) is used to judge the local smoothness of the numerical solution and switch between the two discretizations.

$$\theta = \max\left(\frac{-\nabla \cdot u}{\sqrt{\nabla \cdot u^2 + \nabla \times u^2 + u_0^2/L_0}}, 0\right) \quad \epsilon[0,1] \tag{2.2.7}$$

Terms u_0 and L_0 are fixed velocity and length scales. The sensor is design to be $\theta \approx 0$ in smooth regions and $\theta \approx 1$ in presence of shock waves.
The viscous terms are expanded to Laplacian form, avoiding odd-even decoupling phenomena and approximated with sixth order central scheme. At the i-th node, the numerical discretization of the spatial derivative of the viscous fluxes in the x direction becomes

$$\left[\frac{\partial}{\partial x}\left(\mu \left.\frac{\partial u}{\partial x}\right|_i\right)\right]_i = \frac{1}{\Delta x^2}\sum_{l=-L}^{L}(a_l^2 \mu_{i+l} u_{i+l} + \mu_i b_l u_{i+l}) \tag{2.2.8}$$

where b_l are the the finite-difference coefficients for the second derivative of order 2L.
From the discretization of the spatial derivatives, the following semi-discrete system of ordinary differential equations is obtained:

$$\frac{\partial \mathbf{w}}{\partial t} = \boldsymbol{R}(\mathbf{w}) \tag{2.2.9}$$

where $\mathbf{w} = [\rho, \rho u, \rho v, \rho w, \rho e]$
The propagation in time of the system is achieved using a three-stage, third-order Runge-Kutta calculation:

$$\mathbf{w}^{(s+1)} = \mathbf{w}^{(s)} + \alpha_s \Delta t \boldsymbol{R}^{(s-1)} + \beta_s \Delta t \boldsymbol{R}^{(s)} \tag{2.2.10}$$

where s=0,1,2 is the sub-step, $\mathbf{w}^(0) = \mathbf{w}^(n)$ and $\mathbf{w}^(3) = \mathbf{w}^(n+1)$ are the solution respectively at the n-th and (n+1)-th steps, $\alpha_s = (0, 17/60, -5/12)$ and $\beta_s = (8/15, 5/12, 3/4)$ are the integration coefficients.

2.3 Fluid-Structure Interface Modeling

In the simulation, the capsule is immersed in the flow field. The no-slip and no-penetration boundary conditions on the surface are imposed using the Immersed Boundary Method (IBM)[27]. This technique simulates the viscous flow with immersed boundaries, discretized with grids that do not conform to the shape of the object. A Cartesian volume grid is generated with no regard to the immersed body which is discretized using a surface grid. The solid boundaries are obtained by the intersection of the surface and volume grid. From now on, with the term Eulerian, the fixed and uniform volume grid is addressed while the moving surface grid will be called Lagrangian.
Since the grid does not conform to the solid boundary, the boundary condition are introduced in the equation by a forcing function. In IBM, two of the most common and successful techniques are the Direct Forcing Approach (DFA) and the Ghost Point-Forcing Method (GPFM)[13]. The first approach incorporates the forcing into the continuos equations, before discretizing. The

source term $S(U) = [0, \rho f_i, \rho f_i u_i]$ simulates the presence of the solid body and it is added in the Navier-Stokes equations thus:

$$\frac{\partial}{\partial t}\begin{pmatrix}\rho\\ \rho u_i\\ \rho e\end{pmatrix} + \frac{\partial}{\partial x_j}\begin{pmatrix}\rho u_i\\ \rho u_i u_j + p\delta_{ij}\\ \rho e u_j + p u_j\end{pmatrix} - \frac{\partial}{\partial x_j}\begin{pmatrix}0\\ \sigma_{ij}\\ \sigma_{ij}u_i\end{pmatrix} = \begin{pmatrix}0\\ \rho f_i\\ \rho f_i u_i\end{pmatrix} \tag{2.3.1}$$

with $f_i = f_i(x,t)$ as the specific forces acting on the element of the boundary. The goal of the method is to design the source term in a way that best represents the immersed body. Even though the DFA is easily implemented and accurate its application in thermal and compressible flows is limited. In fact, the method works only for Dirichlet boundaries conditions, which can be considered fixed. When working with compressible flows, the boundary conditions are often defined as a gradient of some fluid variables. Therefore, it is necessary to work with a method that can deal with both Dirichlet and Neumann boundary conditions. The GPFM method is the one used by STREAmS and works with both boundary conditions.
The Ghost Point-Forcing Method imposes the boundary condition on the body interface using the ghost points: these are points in the solid that have at least one neighbour in the fluid region. It follows that the method needs to discern the nature of the point. This is done by an automatic solid detection technique based on the ray tracing algorithm. The three dimensional surface is discretized with triangular elements collected in Σ. Denoted with x_o the grid point to discern and $\bar{x}$ a point lying at reasonable distance from x_0 in the outer region, a semi-infinite ray R(t) starting from x_0 is defined as

$$R(t) = x_0 + (\bar{x} - x_0)t \quad t\epsilon[0:1] \tag{2.3.2}$$

This ray is used inside a loop to identify any intersections with all elements in Σ. Based on Jordan's theorem, in the total number of intersections is even, the grid point x_0 is outside the surface and is labelled as a fluid point otherwise it is considered a solid point. Once the distinction is made, the ghost points are obtained by looking for fluid points in the neighbourhood of a solid point: if at least one fluid point is detected, the selected solid point is labelled as ghost point.
In order to ensure the desired boundary condition at the fluid, the definition of the boundary and image points in the flow is necessary. in figure 2.4 a representation of the procedure is shown. Considering a ghost point x_g, the first step is the identification of the nearest Lagrangian points. Once these two points are spotted, the line $\mathcal{L}$ passing through them and the relative orthogonal direction $\boldsymbol{n}$ are defined. The boundary point has to be located along the orthogonal line to $\mathcal{L}$, passing through the ghost point. Therefore this point corresponds to the intersection of the two lines. The location of the image point is determined using the expression

$$x_{ip} = x_g + 2n_b\|x_b - x_g\| \tag{2.3.3}$$

where n_b is unit vector associated with the normal outer direction at the boundary location.

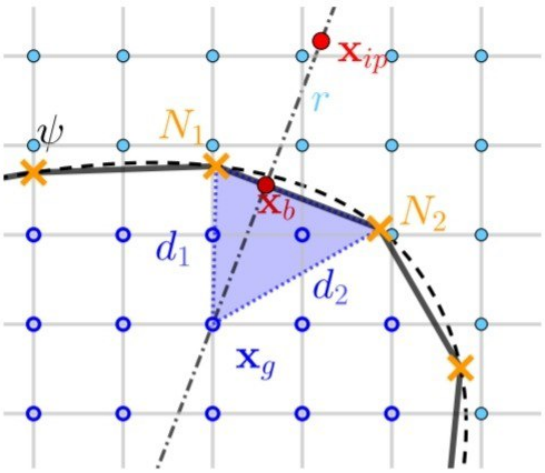

Figure 2.4: Sketch of the determination of the boundary point x_b and image point x_ip, in respect of a ghost point x_g. The blue circles are the ghost nodes, the orange crosses the Lagrangian points and the light blue points the fluid region [13]

The values of the flow field variables at each image point are interpolated from the surrounding grid points and used to settle the values at the corresponding ghost points. In this way, the desired boundary conditions at the fluid-solid interface are ensured.

Chapter 3

Results

In this section, a comparison between the simulation's results obtained at Mach number 2 and 5 is made for the instantaneous, mean and root mean square fields, with a 0° angle of attack. In addition, the modal analysis is carried out using the Proper Orthogonal Decomposition (POD). Mach 2 corresponds to the opening of the parachute while Mach 5 is more or less the middle of the entry sequence, which starts at Mach 25 and lasts around three minutes as seen from table 3.1, which represents part of the trajectory points obtained by COMARS+ measurements during the descent [16].

Trajectory point	Flight time [s]	Altitude above ground [km]	Speed [m/s]	Mach number
Entry Interface	0	122.6	6001.39	32.320
S1	35.553	82.467	5829.38	27.946
S5	145.551	20.862	1236.92	5.431
S6	155.551	18.887	1001.92	4.360
S10	195.551	11.379	503.09	2.120

Table 3.1: Trajectory points with related flight time, altitude, speed and Mach number. The points considered are the one relative to the atmospheric entry at Mach 5 and Mach 2

The non-dimensional formulation is implemented so that the findings represent the variations of the flow field variables with respect to the upstream values. These quantities are therefore expressed as a ratio between the resulting quantity and the freestream condition, denoted with the subscript ∞. The freestream values are listed in the table below and are obtained from the COMARS+ measurements [16].

Density ρ_∞	$2.962 \times 10^{-3} Kg/m^3$
Pressure P_∞	114.57 Pa
Temperature T_∞	202 K
Sound velocity a_∞	257 m/s

Table 3.2: Atmospheric parameters adopted as freestream conditions

The martian atmosphere is considered as purely made of CO_2 [11], idealized as a calorically perfect gas, with ratio of the specific heat constant at $\gamma = 1.33$. Using the Mathematica software to obtain the function that describes the behavior of the specific heat at constant pressure for

a thermally perfect gas, and then comparing these data with the theoretical value obtained from the definition of specific heat, table 3.3 is obtained. The reference temperature is the one obtained form Schiaparelli measurements during its descent at Mach 5 [16] and the value of the specific gas constant for the CO_2 $R = 188.92 \frac{kJ}{kgK}$.

	Cp [J/mol K]	γ
calorically perfect gas	761.405	1.33
thermally perfect gas	743.448	1.34

Table 3.3: Comparison between the specific heat at constant pressure obtained for a calorically perfect and a thermally perfect gas at T=202.28 K

It is clear then that for this simulation, approximating the atmosphere as a calorically perfect gas is correct since the real and theoretical values of the thermal constants do not change significantly. In fact, the relative error of the Cp measure is 2.358%, below the maximum engineering acceptable value of 3%.
The simulation is carried out on CINECA's Marconi100 cluster, allowing the parallel computing of the domain on 32 GPUs. The in-house solver STREAmS is used, as mentioned above, to reproduces the flow behavior around the capsule. This is a scaled version of the ExoMars descent module, where the diameter d of the larger part is used to normalize the dimensions of the domain. The capsule discretization is shown in figure 3.1. The computational domain is configured as a square cuboid of size $20d \times 10d \times 10d$, discretized using a Cartesian non-body conformal, structured grid. The mesh features $2048 \times 672 \times 672$ grid point, for a total of 924 844 032 nodes. It is important to note that, as it is shown in figure 3.2 the distribution of the grid points is not uniform but is thicker in the area around the capsule. The non-uniform distribution allows to capture the intense gradients that characterize the turbulent wake region. Inside this grid the capsule is positioned in a way that, considered the tip of the front shield the origin of the x-y-z reference system,the coordinates of the domain are $[-1, 19] \cdot [-5, 5] \cdot [-5, 5]$. The shape of the boundary is provided through a triangulated surface in the standard STereo-Lithography (STL) format and the simulation was carried out using Reynolds number $Re = 1 \times 10^6$ and WENO 7.

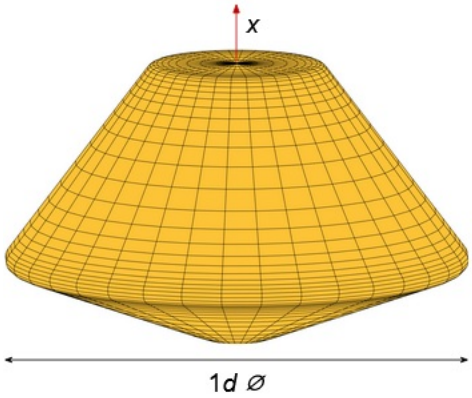

Figure 3.1: Capsule discretization

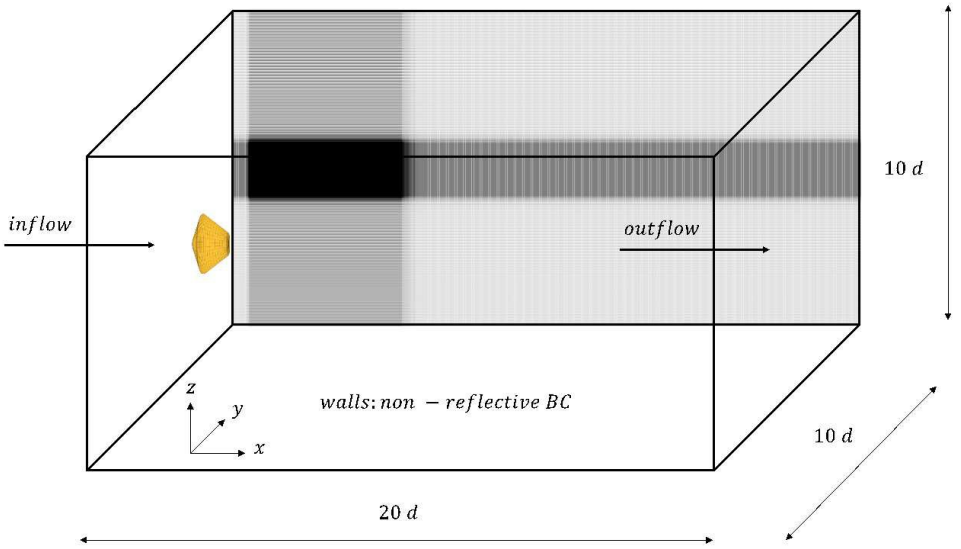

Figure 3.2: Domain discretization.

Before diving into the discussion of the results, these are checked with the theoretical data obtained using the Shock Expansion Theory. The following table shows both the theoretical and experimental values of density, pressure and temperature after the point of the bow shock which corresponds to the symmetry axis of the capsule, where the shock can be considered as a normal shock.

Quantity	Teoretical	Simulation	Relative Error
Density ρ/ρ_∞	6.0526	5.9546	1.6191%
Pressure P/P_∞	28.1304	28.1996	0.2460 %
Temperature T/T_∞	4.6476	4.7359	1.8999%

Table 3.4: Density, Pressure and Temperature calculated using the Shock Expansion Theory Vs the values acquired during the Mach 5 simulation. These non-dimensional data are referred to the wave in front of the nose of the capsule.

The comparison shows that the Shock Expansion Theory can still be applied to describe the shock wave originated by a capsule entering the martian atmosphere at Mach 5. Looking at the relative errors, these are below 3%, a value above which, as previously explained, the measurement is not considered valid.

3.1 Instantaneous fields

Figures 3.3 and 3.4 show the instantaneous density, pressure, temperature and entropy obtained from the simulation, respectively at Mach 2 and Mach 5. First, it can be noticed that as the Mach increases, the shock wave closes up more around the capsule and its distance from the nose of the capsule decreases.
Knowing that, in the freestream the only thing that changes, in the two cases, is the velocity, some considerations about the intensity of the shock can be made. While the shock at Mach 5 is more intense than the one occurring at Mach 2, the qualitative behavior of the flow right after the shock is the same. Around the nose, where the shock can be considered normal, there is

the highest jump in density, pressure and temperature which then decrease with the increasing angle of the shockwave. This behavior is explained by the Shock Expansion Theory, where the bow shock is described as a combination of normal and oblique shocks. Density, pressure and temperature before and after the shock are related by a function of the normal Mach, which decreases with the increasing angle β (equation 3.1.1). This angle represents the inclination of the wave with respect to the horizontal axis. So, looking back at the figures, starting from the point in the shock wave where z=0 and moving along it, its inclination increases hence the decrease in the intensity of the density, pressure and temperature variations.

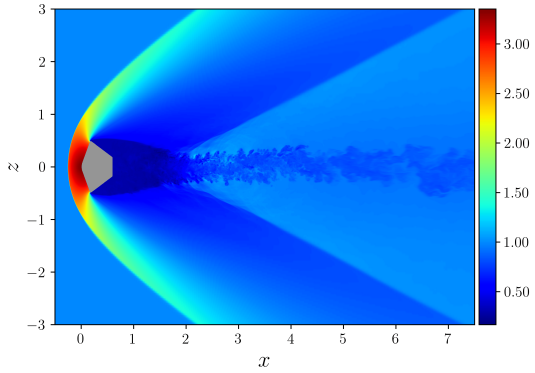

(a) Instantaneous density ρ/ρ_∞

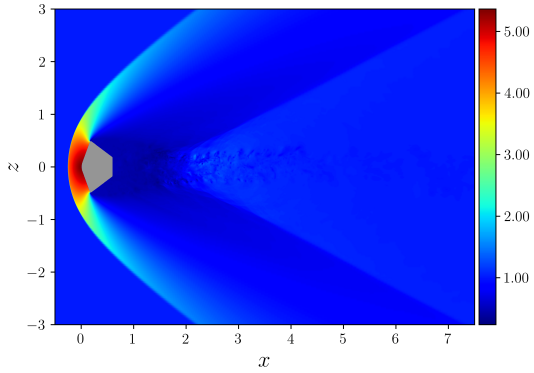

(b) Instantaneous pressure P/P_∞

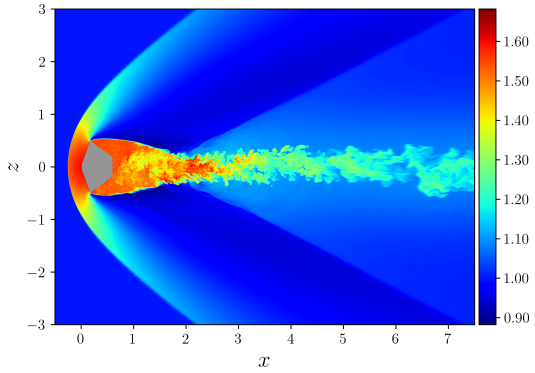

(c) Instantaneous temperature T/T_∞

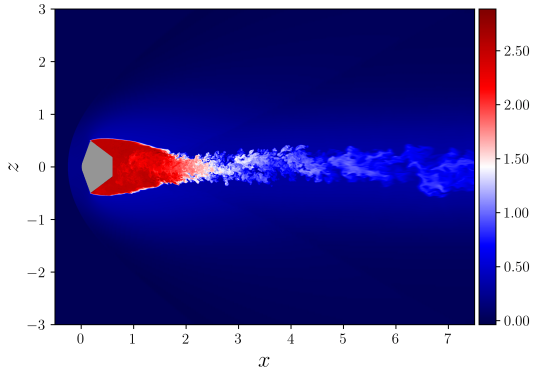

(d) Instantaneous entropy $S - S_\infty$

Figure 3.3: Instantaneous fields around the capsule at M=2, obtained from an x-z slice of the domain. The density, pressure, temperature and entropy are shown in the zone field around the capsule, with x/D between -0.45 and 7.5

The Shock Expansion Theory can also explain the big difference in the intensity of these jumps between the Mach 2 and Mach 5 case. As stated before, the relationships between the quantities before and after the shock wave is a function of the square of the normal Mach. So it is clear that, at the same β, when the value of Mach is higher also the intensity of the quantities' drastic change is greater. This is expressed, for example, by equation 3.1.2, where the relationship between the pressure after the shock, P, and the freestream value P_∞ is shown as a function of the normal Mach, obtained by equation 3.1.1

$$M_n = M sin\beta \tag{3.1.1}$$

$$\frac{P}{P_\infty} = 1 + \frac{2\gamma}{\gamma + 1}(M_n^2 - 1) \tag{3.1.2}$$

The differences between the two cases start right after the shock wave. Looking at the temperature (figures 3.3c and 3.4c) this difference becomes more evident. For Mach 2 case, the flow is subjected to an expansion and recompression that allow it to get back to the undisturbed condition. The turbulent section formed right after the capsule originates the turbulent wake with a neat distinction from the rest of the field. In contrast, when looking at the case at Mach 5, this sharp distinction does not occur. After the shock, in the area around the capsule, the flow is not uniform and this inhomogeneity continues also around the tail. This means that the flow never reaches the freestream conditions after the shock. The reason behind the fact that the undisturbed conditions are never reached after the shock wave when considering Mach 5 is explained by looking at the entropy. This quantity, defined as a difference between two thermodynamic states, is obtained knowing the temperature and the pressure (equation 3.1.3,expressed for the non-dimensional analysis) and it is shown in figures (3.3d) and (3.4d).

$$S - S_\infty = \frac{\gamma}{\gamma - 1} \ln \frac{T}{T_\infty} - \ln \frac{P}{P_\infty} \tag{3.1.3}$$

While in the first picture only the turbulent region is shown, in the one corresponding to the entropy at Mach 5, a wider area is shown. This corresponds to the inhomogeneity present in the other fields. Some instabilities are therefore present and these make the compression process performed by the wave more irreversible than the Mach 2 case.

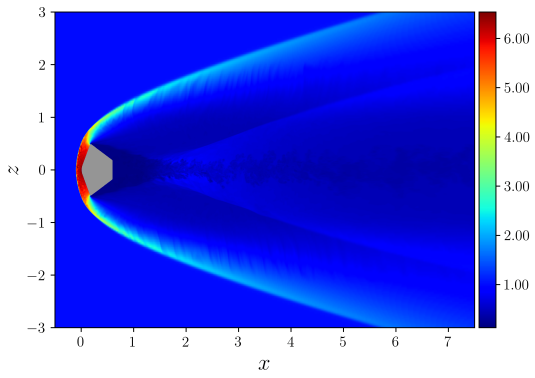

(a) Instantaneous density ρ/ρ_∞

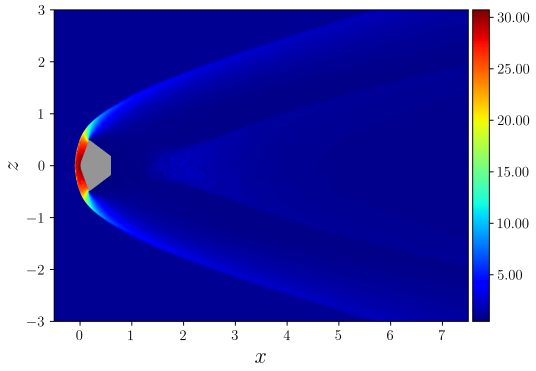

(b) Instantaneous pressure P/P_∞

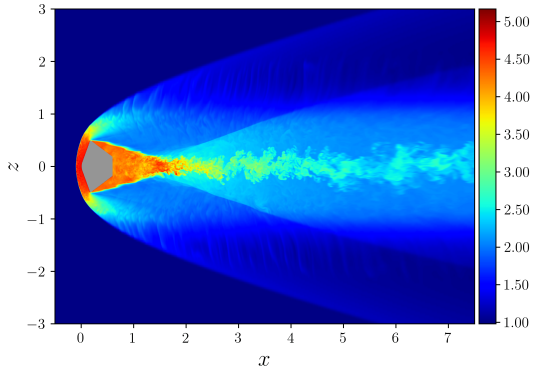

(c) Instantaneous temperature T/T_∞

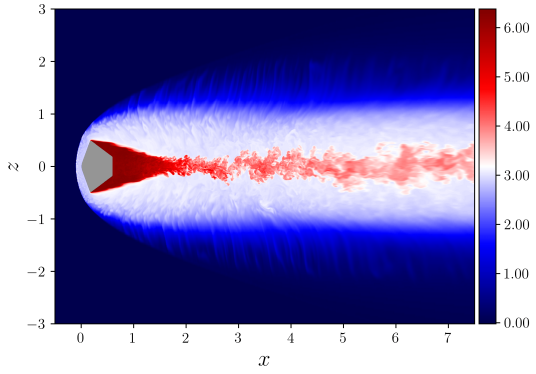

(d) Instantaneous entropy $S - S_\infty$

Figure 3.4: Instantaneous fields around the capsule at M=5, obtained from an x-z slice of the domain. The density, pressure, temperature and entropy are shown in the zone field around the capsule, with x/D between -0.45 and 7.5

Looking at figure 3.5, where the instantaneous Mach field is shown for both cases, it is possible

to observe what it is already been said. The red line represents the point where the flow reaches the sonic condition. The region between the shock wave and the sonic line is, in both cases, what is expected from the theory. The irregularity observed in the other fields is also present here and it is shown that it continues along the total length of the domain. It is also possible to observe that the turbulent zone right after the capsule goes back to the sonic condition faster when the initial flow is faster.

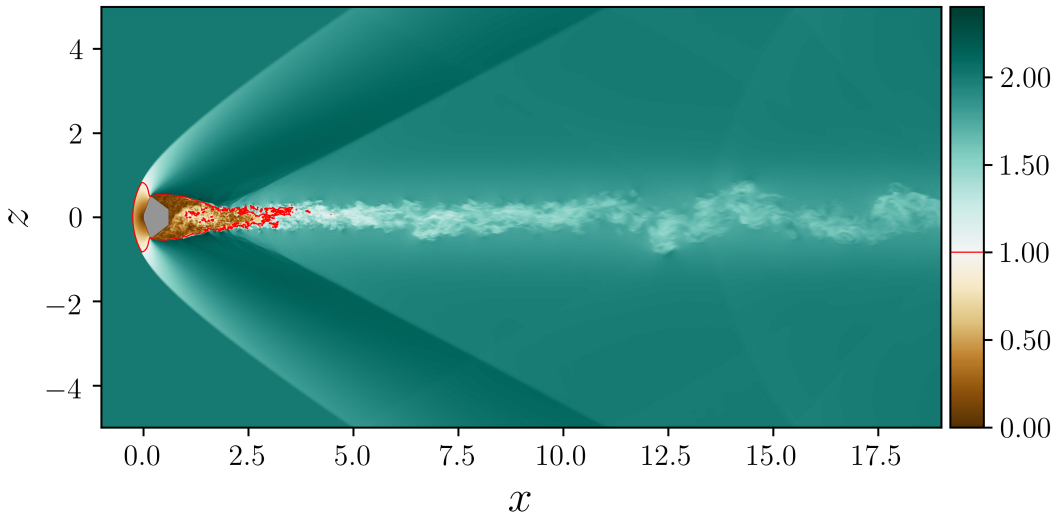

(a) Instantaneous Mach field around the capsule at M=2.

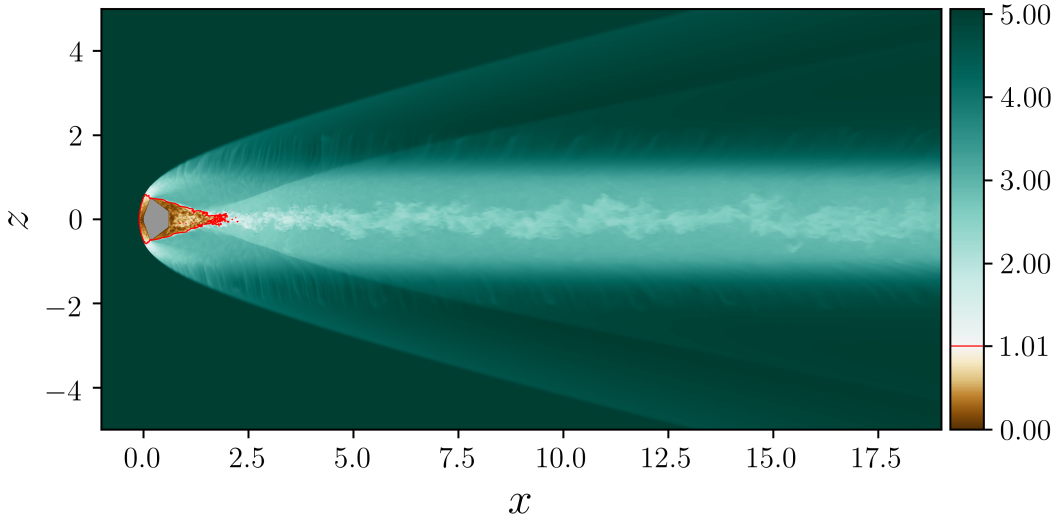

(b) Instantaneous Mach field around the capsule at M=5.

Figure 3.5: Instantaneous Mach field around the capsule at different values of Mach. In red is represented the sonic line, where the flow reaches the sonic condition M=1.

The reason why in the Mach 5 case, there are perturbances that make the shock wave an irreversible phenomenon, is explained by looking at figure 3.6. Here the components along the y-direction of the vorticity, obtained for the two cases, are displayed in the x-z plane. This quantity, obtained as the rotor of the velocity (equation 3.1.4), describes the local spinning motion of a continuum near some point as would be seen by an observer located at that point

and traveling along with the flow. The presence of vorticity implies a turbulent flow and a consequent energy dissipation.

$$\overline{\omega} = \overline{\nabla} \times \overline{V} = (\frac{\partial w}{\partial y} - \frac{\partial v}{\partial z})\hat{x} + (\frac{\partial u}{\partial z} - \frac{\partial w}{\partial x})\hat{y} + (\frac{\partial v}{\partial x} - \frac{\partial u}{\partial y})\hat{z} \tag{3.1.4}$$

Looking at the plots, the different situation is pretty clear: while for Mach 2 the vorticity is present only in the recirculation region and the turbulent wake, for Mach 5 there is vorticity starting from the shock wave and it propagates around the capsule and the turbulent wake. This high vorticity is here attributed to the non-isentropic flow induced by the hugh Mach bow shock via the Crocco mechanism. From the insert, it is seen that the vorticity in front of the capsule is present also in the first case but its value is low and it disappears right away, contrary to what happens in the second case. Here the value of vorticity is high and moving along x it decreases but does not go to zero. This turbulent flow causes the energy loss that is represented in the entropy field.

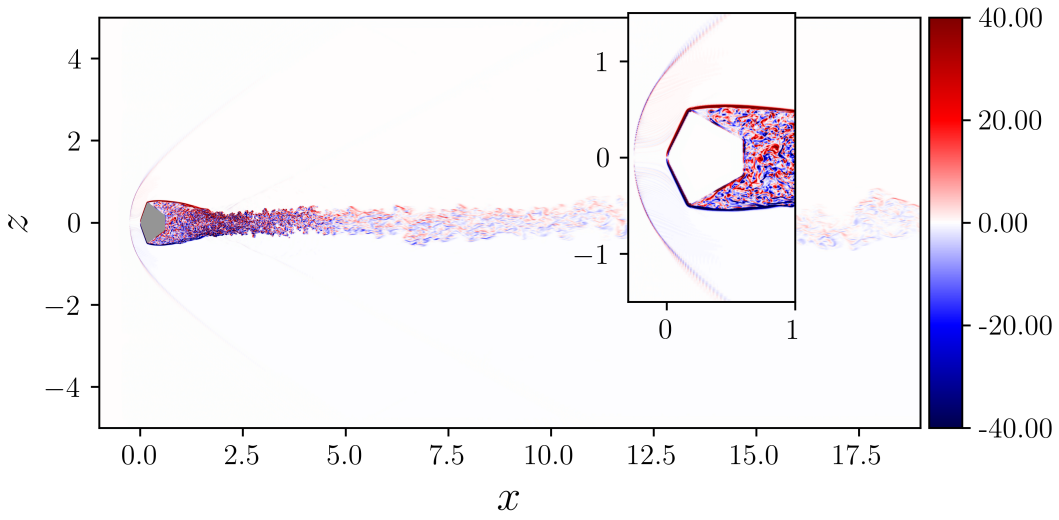

(a) Vorticity around the capsule at M=2.

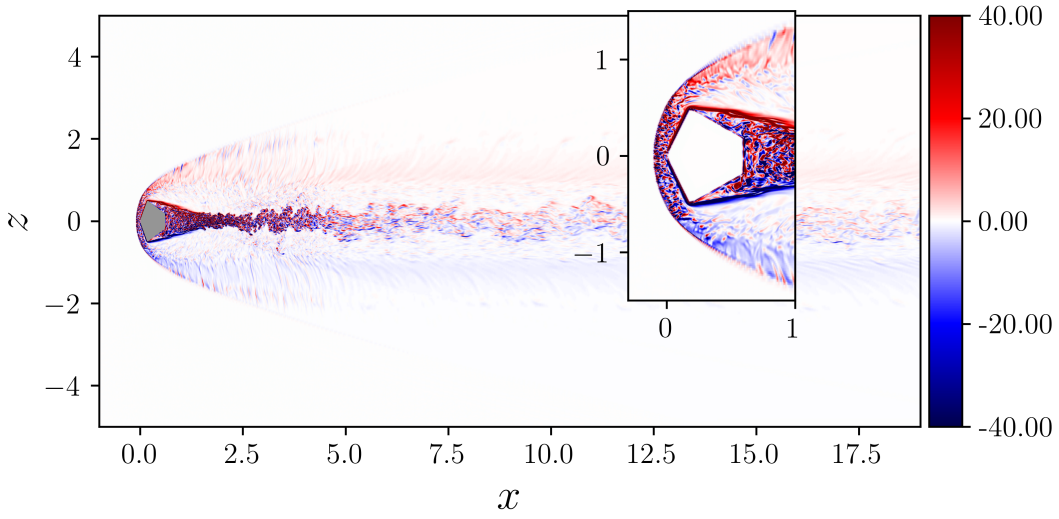

(b) Vorticity around the capsule at M=5.

Figure 3.6: Vorticity around the capsule at different values of Mach. An insert shows a close-up of the behavior of the vorticity between the shock wave and the capsule.

3.2 Mean fields

In this section are shown the plots obtained from a set of 757 x-z slices of the domain, considering only the ones after the end of the transitional phase. Each slice is obtained with a time step of $2 * 10^{-2}$, for a total of 15.2 units of time. [1]

3.2.1 Two-dimensional slices

Figures 3.7 and 3.8 show the mean density, pressure, temperature and entropy fields obtained from the simulation, respectively at Mach 2 and Mach 5. Considerations made for the instantaneous fields also apply to the mean fields. In fact, from the pictures, it is clear that the trends followed in figures 3.3 and 3.4 by the flow are the same as the one shown here, with the only difference being in the turbulent regions, due to the averaging process itself. The turbulence fluctuates over time and the averaging process eliminates these fluctuations.
In addition, figure 3.8d shows that the entropy in Mach 5 case is still nonzero around the capsule, implying that the vorticity is still present.

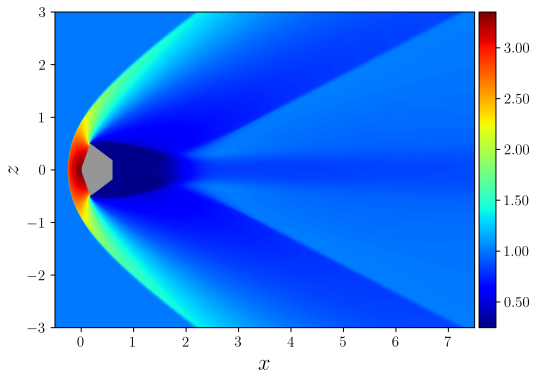

(a) Mean density $\bar{\rho}/\rho_\infty$

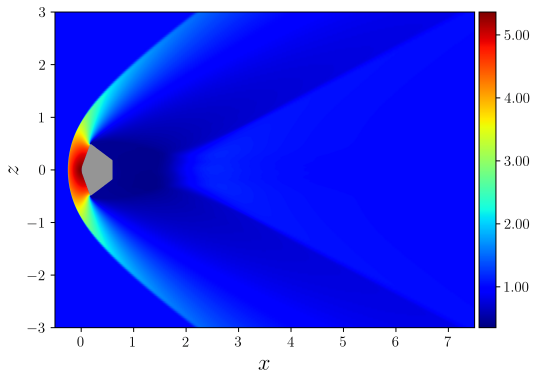

(b) Mean pressure $\bar{P}/P_\infty$

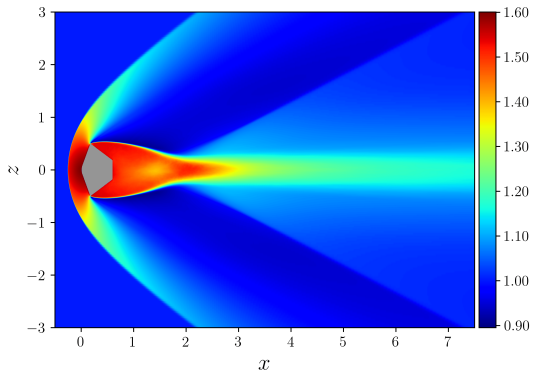

(c) Mean temperature $\bar{T}/T_\infty$

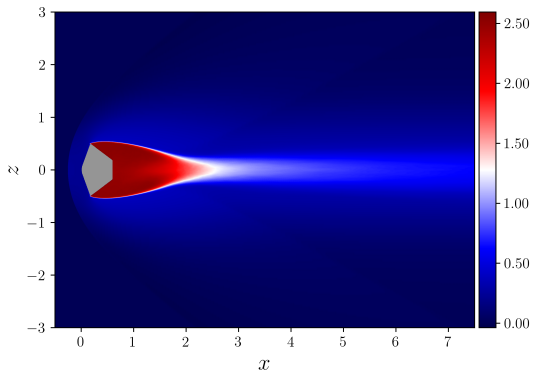

(d) Mean entropy ΔE

Figure 3.7: Mean fields around the capsule at M=2, obtained from x-z slices of the domain. The density, pressure, temperature and entropy are shown in the zone field around the capsule, with x/D between -0.45 and 7.5

[1] in the non-dimensional analysis also the time has been nondimensionalized

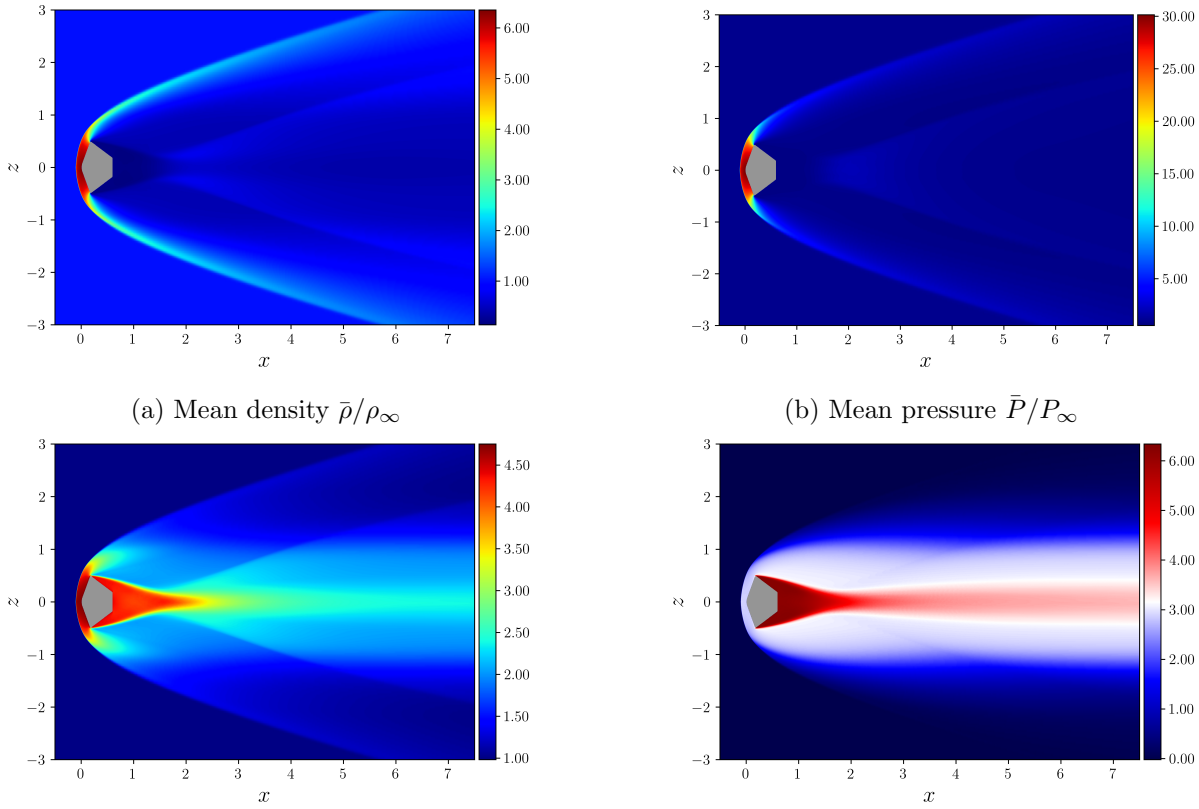

(a) Mean density $\bar{\rho}/\rho_\infty$

(b) Mean pressure $\bar{P}/P_\infty$

(c) Mean temperature $\bar{T}/T_\infty$

(d) Mean entropy ΔE

Figure 3.8: Mean fields around the capsule at M=5, obtained from x-z slices of the domain. The density, pressure, temperature and entropy are shown in the zone field around the capsule, with x/D between -0.45 and 7.5

Looking at the mean temperature, the higher value in the Mach 5 case is expected because, using the atmospheric drag to decelerate, the kinetic energy of the capsule is dissipated by heating up the gas around it. This means that the greater the velocity, higher the quantity of energy to transform into heat, therefore the gas around the capsule will be hotter.
In figure 3.9 the mean Mach field is shown for both cases. Here it is much easier to observe that the flow can get back to the pre-shock conditions when the initial Mach is 2 with exception of the wake region, while in the other case the area where the flow is not at freestream conditions is wider. The red line represents when the flow reaches the sonic condition. As already seen for the instantaneous fields, the subsonic region after the capsule is shorter at a higher value of Mach.

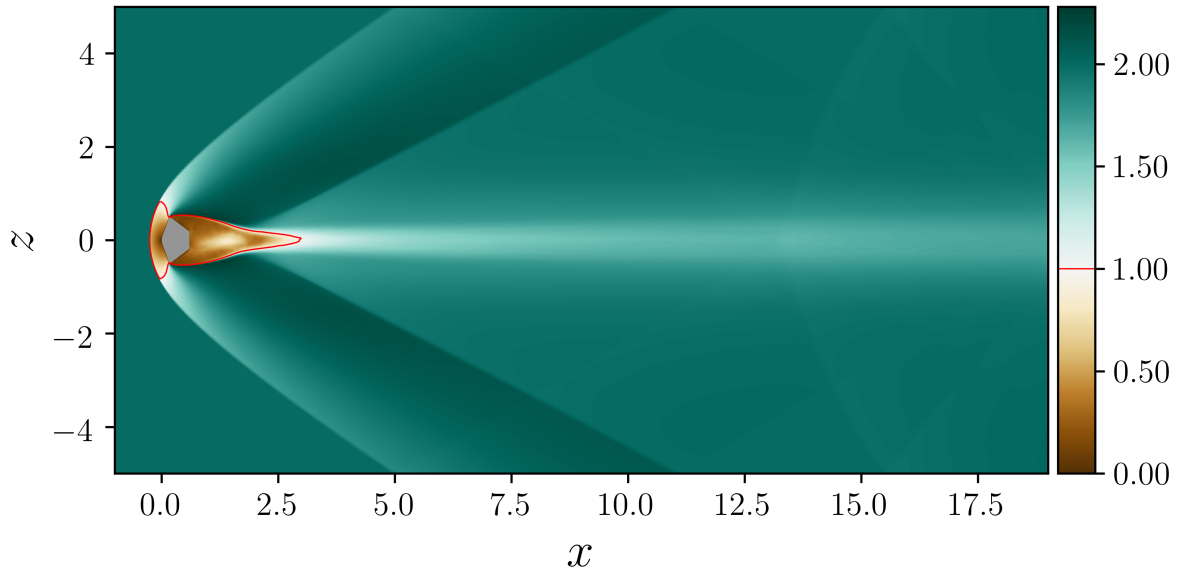

(a) Mean Mach field around the capsule at M=2

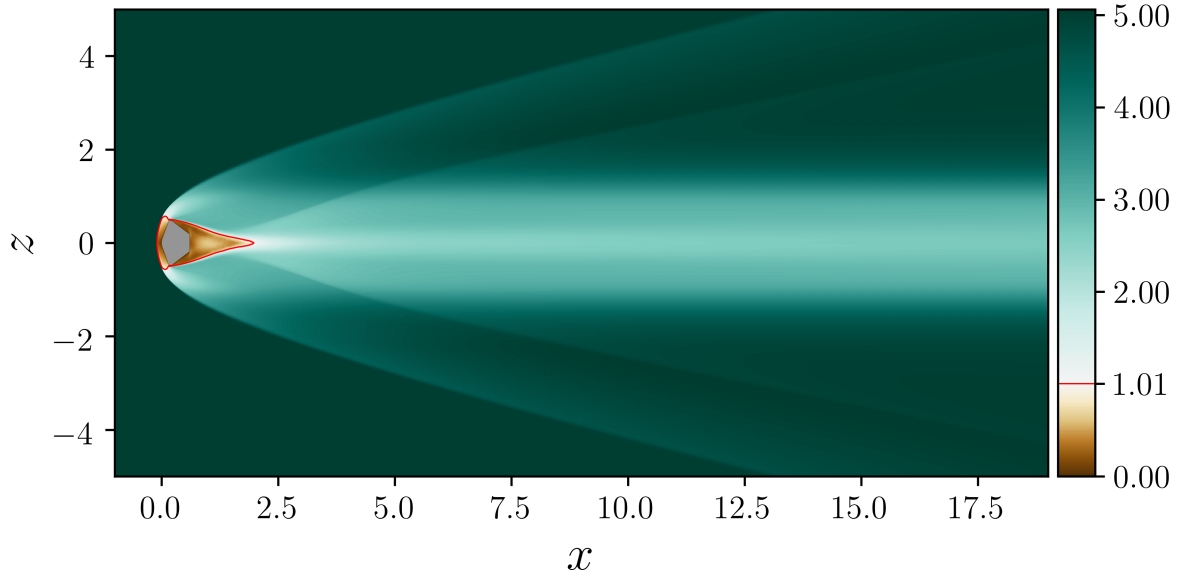

(b) Mean Mach field around the capsule at M=5

Figure 3.9: Mean Mach field around the capsule at different values of Mach. In red is represented the sonic line, where the flow reaches the sonic condition M=1

3.2.2 Qualitative study

Figure 3.10 shows the theoretical flow field of a supersonic flow field around the OREX capsule, a Japanese technology demonstrator whose shape is similar to the ExoMars one. The OREX capsule, Orbital Re-entry Experiment, launched in 1994, was used to acquire re-entry data during an atmospheric descent on Earth. It has a blunt-cone shape, with nose radius of 1.35m, twice the one of Schiaparelli[6]. The flow field after the shock wave is characterized by the sonic line, the expansion wave, the recompression shock and the wake trail. Each of these

lines represents a drastic variation of pressure, temperature, density and velocity of the fluid. Therefore the flow is divided into different zones. The zone bounded by the shock wave and the sonic wave is characterized by a subsonic flow. Outside this region, the flow is supersonic and the velocity increases as the wave decreases in intensity. The change in geometry at the shoulder of the capsule induces the formation of expansions waves which accelerates the flow. Here there is also the separation point, where the boundary layer detaches, forming a free shear layer that separates the inner recirculating flow from the outer flow field. The recirculating region, positioned behind the capsule, is characterized by an inversion of the velocity and it ends with the development of the wake trail. Where this happens, the outer flow is subjected to a recompression shock which turns the flow back to the freestream conditions.

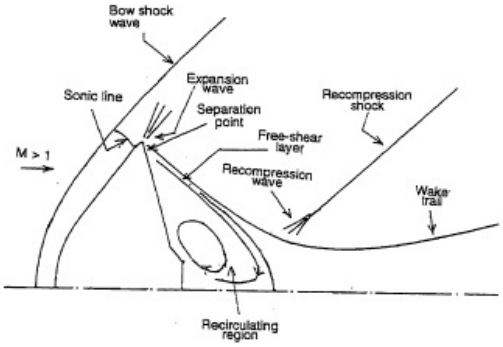

Figure 3.10: flow field field around OREX capsule [24]

The objective of the qualitative study is to identify the features listed above in the Mach distribution and to compare the findings obtained for Mach 2 and 5. This is done by tracing the contours of different Mach numbers for both fields. Figure 3.11 shows the mean Mach fields with the relative contour. In figure 3.11a, are outlined the curves for Mach 1,1.5 and 1.99, while in figure 3.11b are traced the contours for Mach between 2.5 and 4.75. In both cases, the red line represents the sonic condition and the maximum value of Mach does not coincide with the freestream value since the number of curves that are shown for M=2 in the first case and M=5 in the second, make the image hard to read. From a first glance it is possible to see that there are big differences between the two images. While in figure 7.a it is possible to observe a clear distinction between the zones, in figure 7.b this distinction is not so neat. The expansion wave, represented by the line corresponding to M=1.99 in the first picture, is not present in the second case while the recompression shock, which should correspond to the coalescence of waves, is obtained as a sequence of these. These differences are due to the already explained non-zero vorticity in the shock region and its propagation in the flow, at Mach 5.

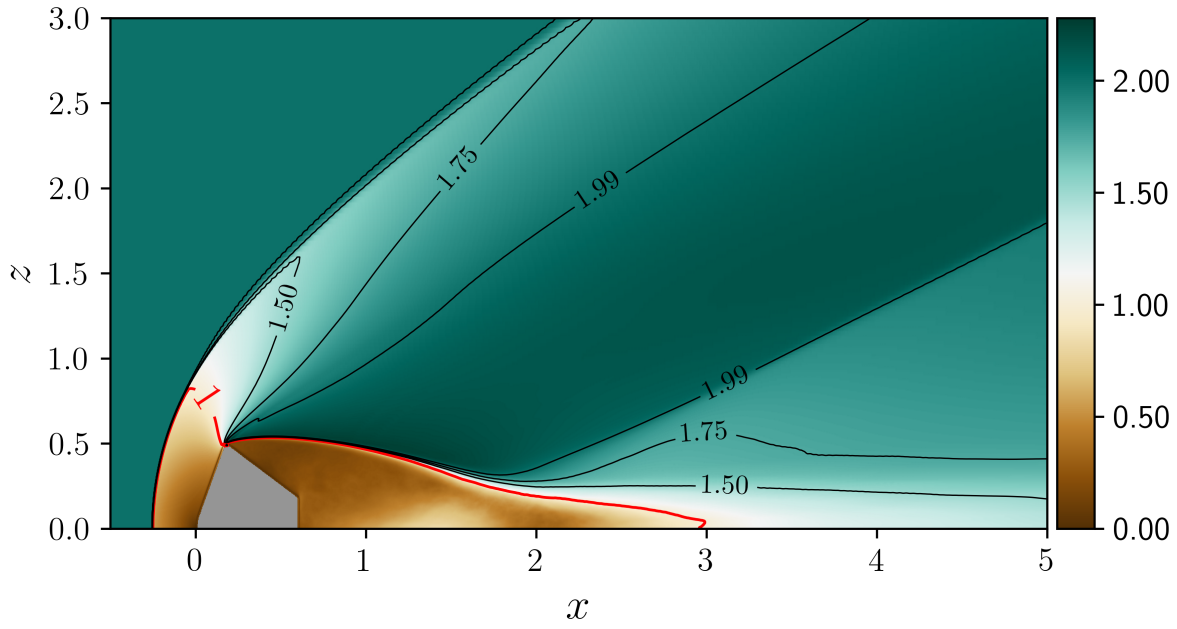

(a) Mean Mach field contour around the capsule at M=2

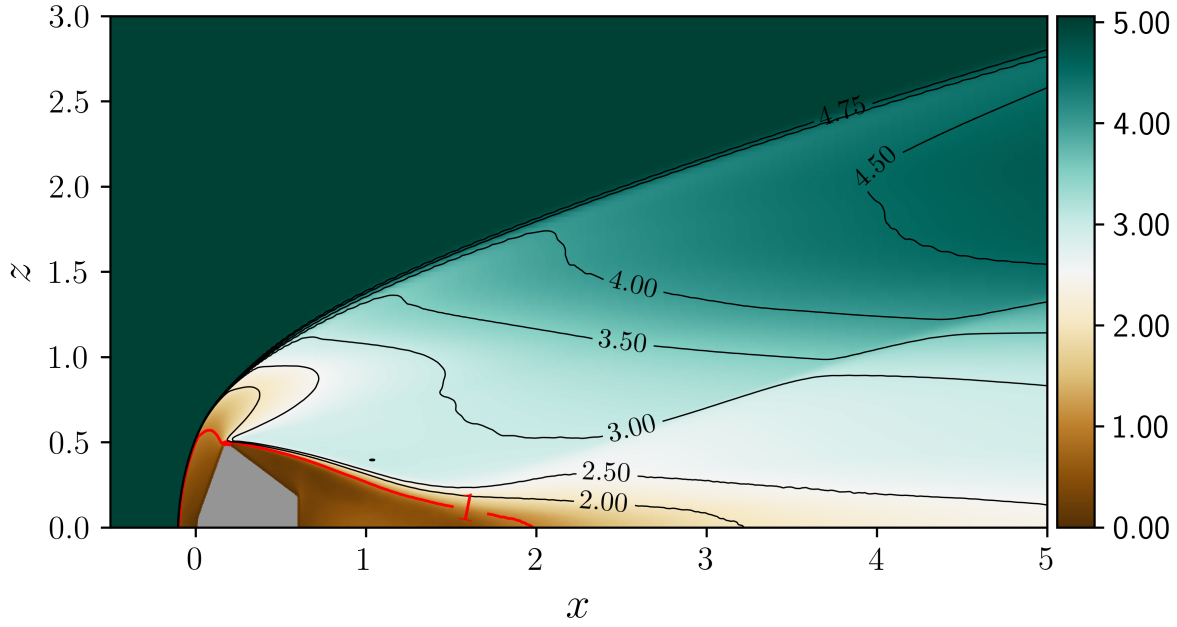

(b) Mean Mach field contour around the capsule at M=5

Figure 3.11: Contour of mean Mach field around the upper half of capsule at different values of Mach. In red is represented the sonic line, where the flow reaches the sonic condition M=1, while in black are indicated, respectively, values of Mach equal to [1.5;1.7;1.99] (a) and [2;2.53;3.5;4;4.5;4.75] (b)

Observing these two figures, it is seen that the subsonic region in front of the capsule reaches a lower value of z, slightly passing the shoulder of the capsule, at Mach 5 compared with the Mach 2 case. This is demonstrated in figure 3.12 where a zoom-in of plot 3.11b is shown together with

the result obtained by computing the flow over a 70° cone, using Euler equations with Mach 5 and specific heat ratio equal to 1.3. This computational process, done in the article [21], aims to understand the behavior of the flow around the sphere-cone transition found in most entry capsule's geometry. In particular, figure 3.12a, shows the sonic line, also called the sonic bubble, formed for a 70° cone with an inclination of 0° with respect to the flow, recreating the same layout in the simulation.
Observing the two figures, it is seen that the behavior of the sonic line in the simulated field is the same as the one presented in the first picture: both start at the horizontal axis and follow the shock until the point more or less aligned with the shoulder of the capsule. Here the "bubble" starts and ends at the shoulder, point where the front conic part of the capsule is attached to the back. This point is called the sonic point and it represents the point where, as seen in picture 3.10, the boundary layer detaches.

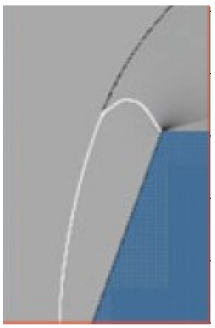

(a) Sonic bubble from [21]

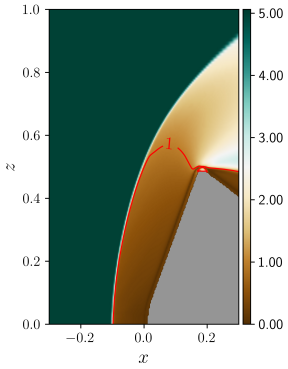

(b) Sonic bubble obtained during the simulation

Figure 3.12: Comparison between the expected sonic bubble (a), obtained by computing the flow over a 70° cone using the Euler equations with M=5 and $\gamma = 1.3$, and the simulated one (b)

3.2.3 One-dimensional approach

The next figure shows the mean density, pressure, temperature and entropy obtained from the simulations, plotted along the axis of symmetry of the capsule, with focus on the section behind the capsule. The freestream condition corresponds to the unitary value. In these graphs, what happens after the capsule represents the middle of the turbulent wake. With exception of the pressure, where both cases tend to get back at the initial undisturbed value, there is a clear difference between the Mach 2 and Mach 5 case. The absolute values of density, pressure, temperature and therefore entropy are greater when the initial Mach is higher, as already discussed in the previous sections.
Considering the subsonic region, the trends followed by the state quantities, in both cases, are characterized by:

- an abrupt drop, right after the end of the capsule, followed by a peak where the sonic condition is reached, for density (a) and pressure (b),

- a peak starting at the end of the capsule followed by a second one when the flow becomes sonic, for the temperature (c)

- a peak right after the end of the capsule followed by a descending trend, looking at the entropy (d)

In particular, the high values of temperature in the recirculation region are due to the dissipation of energy, resulting from the vortex generated in this region.
Moving away from the body, the wake decrease in intensity hence the change of behavior. Looking at the tail, starting from x/D=2.5, the differences start here. First of all, in the Mach 2 case study, the density keeps increasing, with slower pace, until it reaches x/D=13 where a shock wave takes place and the density increases a little bit. This shock wave is visible in figure 3.9a as a faded, light-colored line and its presence affects also the pressure trend in figure (b), where the value slightly increases after reaching the freestream value. When the initial Mach is 5, the shock wave is not present in the wake and the whole behavior in the trail is different. The density, after the sonic line, decreases again and then, where x/D is around 7.5, increases a little. Still, it does not reach the undisturbed value. This behavior is the same shown for the pressure but here, as already observed, the final value is closer to 1 than in the other plots.
Lastly, the temperature (c) and entropy (d), do follow the same trends as the Mach 2 case but with greater absolute value and being far from the upstream values, 1 in the case of the temperature and 0 for the entropy.

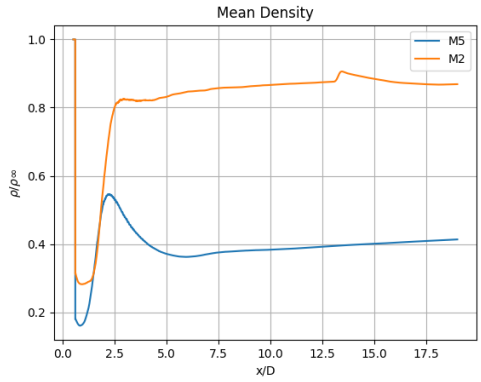

(a) Mean density $\bar{\rho}/\rho_\infty$ along axis of symmetry of the capsule

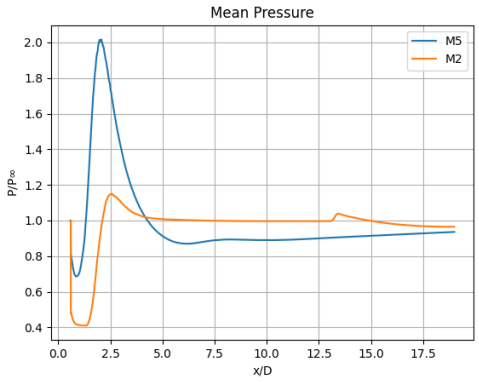

(b) Mean pressure $\bar{P}/P_\infty$ along axis of symmetry of the capsule

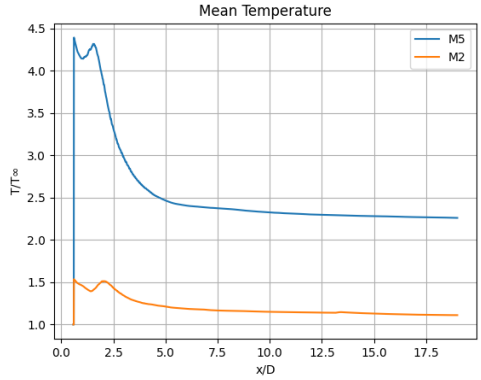

(c) Mean temperature $\bar{T}/T_\infty$ along axis of symmetry of the capsule

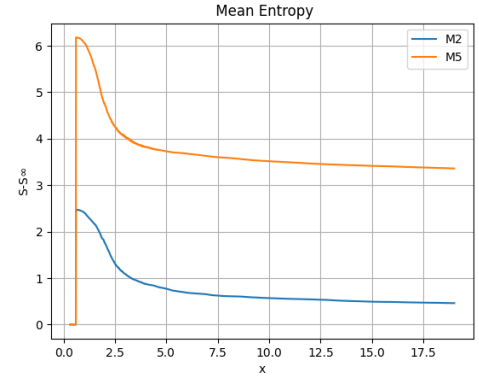

(d) Mean entropy ΔE along axis of symmetry of the capsule

Figure 3.13: Plots that show a comparison between trends of the mean density, pressure, temperature and entropy along the axis of symmetry of the capsule at M=2 and M=5. The focus is on the flow behind the capsule, starting at x/D=0.6

3.3 RMS fields

In the next paragraphs, the analysis is made for the Root Mean Square (RMS) fields,which show the mean intensity of the fluctuations in specific point of the domain and is obtained as the square root of the mean of the squares of the values set. The quantities shown are the same as the instantaneous and mean fields analysis with exception of the entropy. Here, in fact, the Turbulent Kinetic Energy (tke) is shown and represents the mean kinetic energy per unit of mass associated with the eddies in a turbulent flow.

3.3.1 Two-dimensional slices

In figures 3.14 and 3.15 the RMS fields are shown for both Mach 2 and Mach 5 cases. The focus here is on the turbulent areas of the flow which, in Mach 2 flow, corresponds to only the part behind the capsule. As seen in the previous section, in the Mach 5 flow, the presence of vorticity around the capsule induces turbulence in the flow. In figure 3.15 this is represented as a "cloud" that starts with the shock wave but closes up more around the capsule and continues along the entire length considered. As expected this cloud is not present in figure 3.14 and the shock is

barely visible.

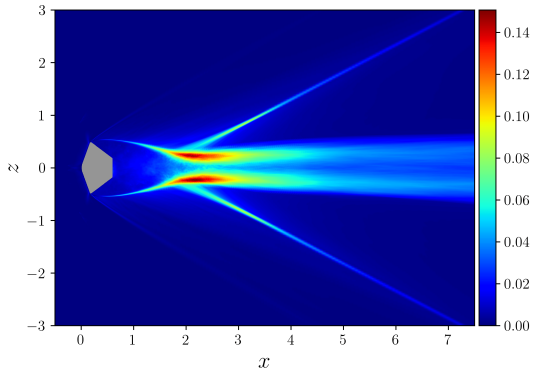

(a) RMS density $\sqrt{\overline{\rho'^2}}$

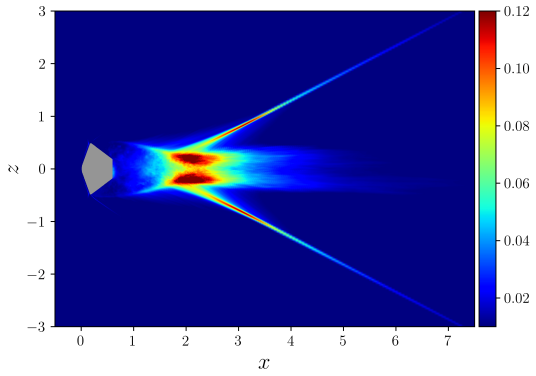

(b) RMS pressure $\sqrt{\overline{P'^2}}$

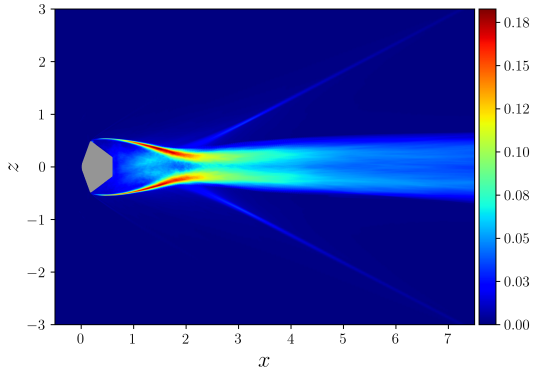

(c) RMS temperature $\sqrt{\overline{T'^2}}$

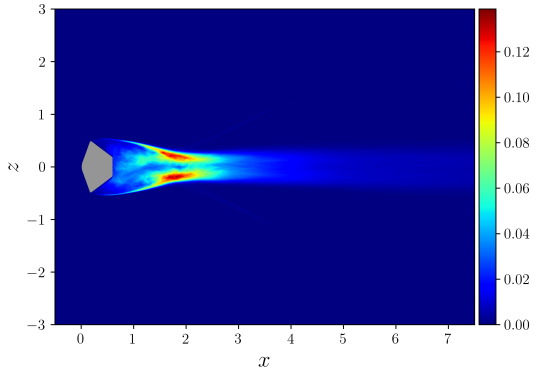

(d) Turbulent kinetic energy $k = \frac{1}{2}\overline{u_i' u_i'}$

Figure 3.14: RMS fields around the capsule at M=2, obtained from x-z slices of the domain. The density, pressure, temperature and entropy are shown in the zone field around the capsule, with x/D between -0.45 and 7.5

Now, focusing the attention on the back cone of the capsule, it is clear that the maximum values are reached where the recompression wave meets the tail and that, along the axis of symmetry of the capsule, there is a division between the symmetrical upper and lower regions. Another aspect that jumps out at the eye is that in the recirculation, for each field considered, the values shown are lower. This implies that the fluctuation is minimal compared to the other regions, being in subsonic conditions.
Considering the turbulent kinetic energy, it follows a different trend than the rest of the fields. In fact as the velocity increases, the turbulent kinetic energy decreases, opposite to what does, for example, the temperature. While the temperature fields show how the turbulence affects the flow, the tke is a measurement of the turbulence itself. In particular, the tke shows how much energy the vortex carries, which decreases as the flow velocity increases.

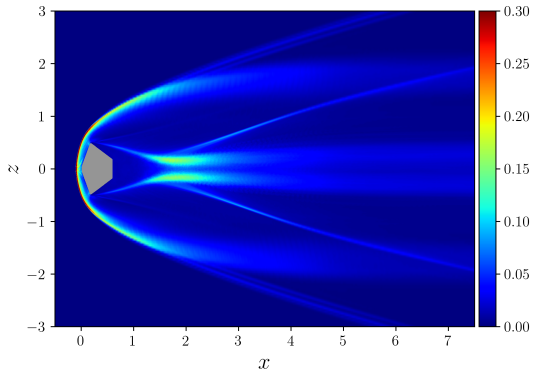

(a) RMS density $\sqrt{\overline{\rho'^2}}$

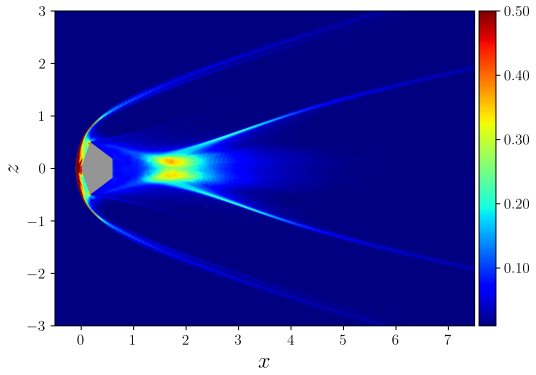

(b) RMS pressure $\sqrt{\overline{P'^2}}$

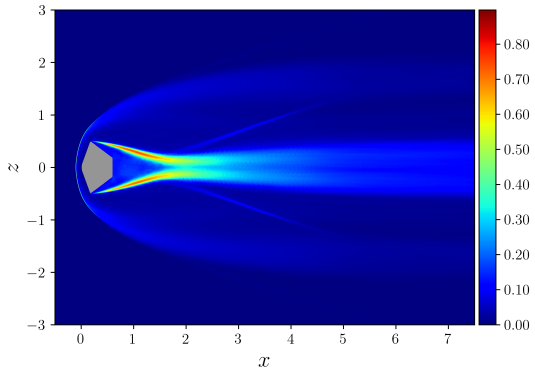

(c) RMS temperature $\sqrt{\overline{T'^2}}$

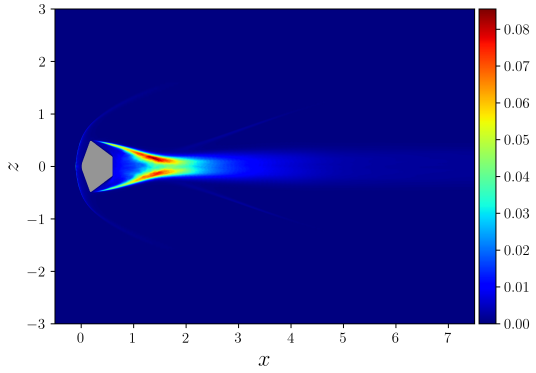

(d) turbulent kinetic energy $k = \frac{1}{2}\overline{u_i' u_i'}$

Figure 3.15: RMS fields around the capsule at M=5, obtained from x-z slices of the domain. The density, pressure, temperature and entropy are shown in the zone field around the capsule, with x/D between -0.45 and 7.5

3.3.2 One-dimensional approach

The following plots show the RMS density, pressure, temperature and turbulent kinetic energy, obtained from the simulations, plotted along the axis of symmetry of the capsule, with focus on the section behind the capsule. The tendency followed is the same in the two cases with a difference in the final value of density and temperature that show a big deviation.
Starting at the end of the capsule, for all the plots, a peak is observed, with maximum where the sonic condition is reached. This is followed by a fast descent that slows down at x/D=5. After that point the lines continue the descent, getting closer to the turbulence cancellation condition. As stated in the previous section, the turbulent kinetic energy is higher for the Mach 2 case, contrary to what happens for the other quantities. In the end, if compared to the maximum values reached by the other parts of the flow shown in figures 3.14 and 3.15, it is clear why the recirculation region was not appreciable since the higher value obtained here is a lot lower.

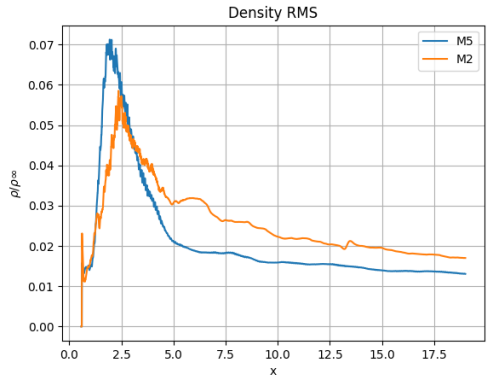

(a) RMS density $\sqrt{\overline{\rho'^2}}$

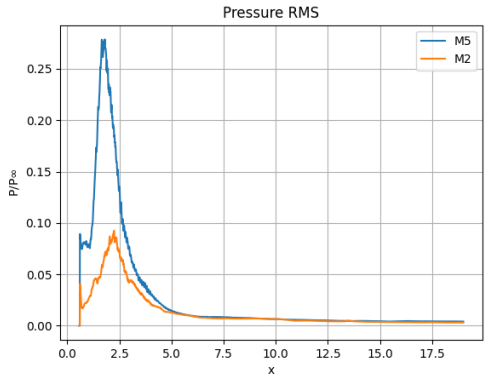

(b) RMS pressure $\sqrt{\overline{P'^2}}$

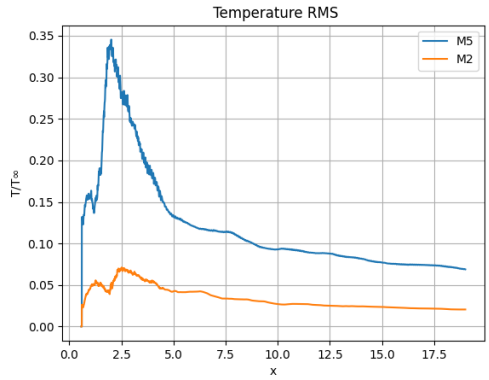

(c) RMS temperature $\sqrt{\overline{\rho'^2}}$

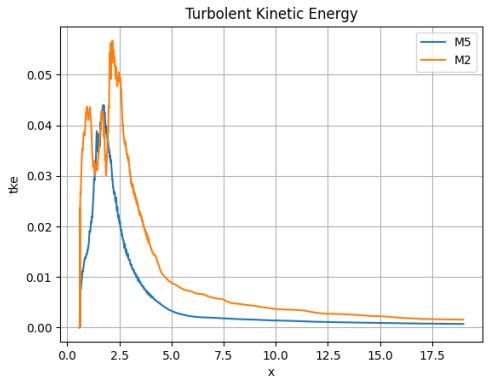

(d) turbulent kinetic energy $k = \frac{1}{2}\overline{u_i' u_i'}$

Figure 3.16: Plots that show a comparison between trends of the mean density, pressure, temperature and entropy along the axis of symmetry of the capsule at M=2 and M=5. The focus is on the flow behind the capsule, starting at x/D=0.6

3.4 Modal analysis

In this section, the Proper Orthogonal Decomposition (POD) analysis is done for the velocity component along the flow direction for the Mach 5 case study. In addition, the first six modes

resulting from the Mach 5 analysis are compared to the ones obtained for the Mach 2 case.
POD analysis searches for a new mutually orthogonal coordinate system which can effectively capture the dominant features of a system, reducing the computational load needed to examine the phenomena being studied. The objective of this type of analysis is to obtain a lower-dimensional description of the flow, considering only the high energy contributions.
The modal decomposition is a mathematical technique used to extract energetically and dynamically important features of the fluid flow, decomposing it into a set of modes [34]. Considered a time interval, the velocity field is discretized and then assembled in a state vector, $\mathbf{q}(\xi, t)$, where ξ is the vector of discrete spatial points. The velocity fluctuation in the original field can be written as

$$\mathbf{q}(\xi, t) - \overline{\mathbf{q}(\xi)} = \sum_{j=1}^{r} a_j(t)\phi_j(\xi \tag{3.4.1}$$

where $\overline{\mathbf{q}(\xi)}$ is the temporal mean, $\phi_\mathbf{j} = [\phi_1, ..., \phi_r]$ is a linearly independent set of modes , defined on the spatial domain, and a_j the time coefficient relative to the r-th mode. The ability to reconstruct the velocity field using the estimated time coefficients a_j, is dependent to the determination of the modes. Therefore the problem is expressed as an eigenvalue problem. In this work, the method employed is the snapshot one: the discretized flow is considered as a series of successive snapshots from which velocity vector is extrapolated. Each vector is used as a column in the definition of the U matrix, which is used, in turn, to defined the matrix $R = \frac{1}{N}UU^T$. Equation 3.4.2 represents the eigenvalue problem and its solution gives both the mode ϕ and the relative energy level λ. [23]

$$R\phi = \lambda\phi \tag{3.4.2}$$

After the modes are found, the flow field can be reconstructed through a linear combination of the computed evolution of each mode in time. As displayed in figure 3.17, the reconstructed model 3.17b is less chaotic than the flow obtained by the LES simulation 3.17a. This is due to the fact that the first mode can be assimilated to the mean velocity field to which the other modes are added, recreating the turbulent flow in its highest energy components. Both figures are relative to the first instant considered and highlight the recirculating region as the one with the fastest flow,together with the turbulence in front of the capsule. It is interesting to observe that, in the second figure, the wake is almost invisible, while in the first is clearly visible. This allows a better understanding on where the energy is dissipated the most, as shown by the entropy field in figure 3.4d.

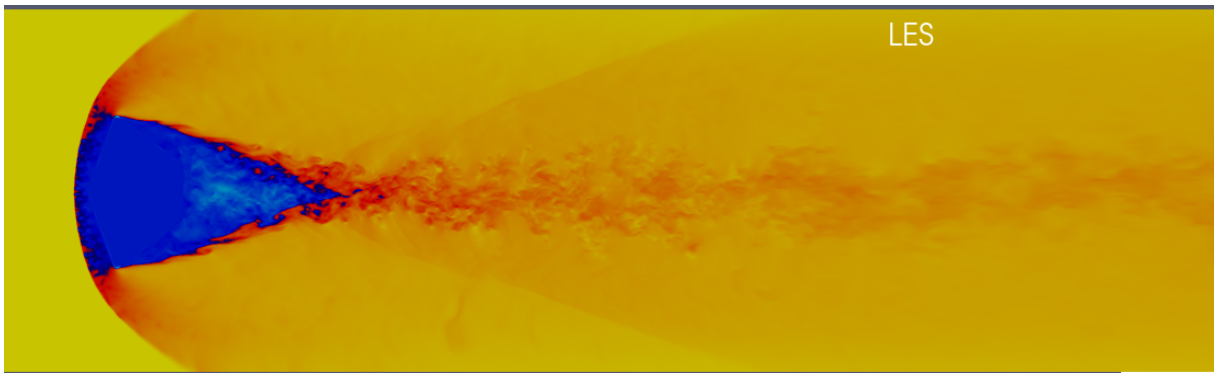

(a) LES representation of the flow, obtained from the simulation

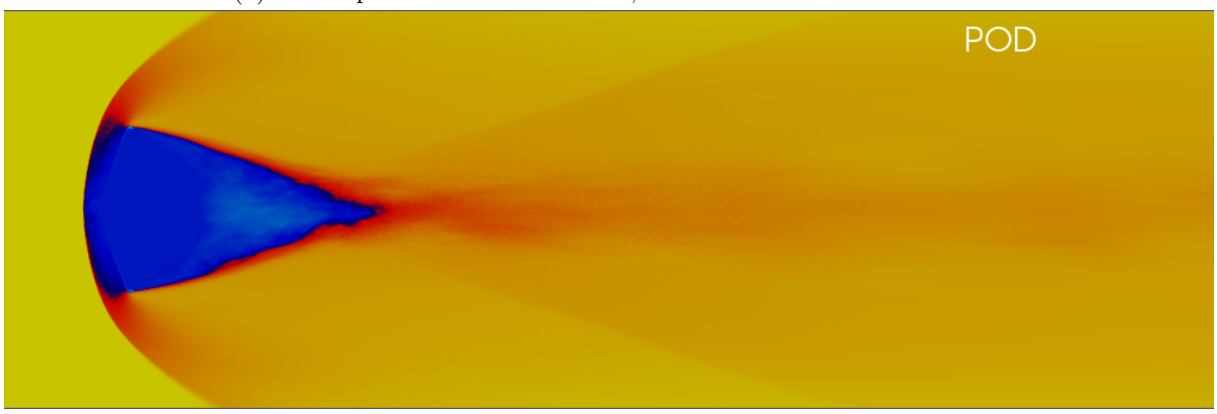

(b) flow reconstruction from the POD analysis

Figure 3.17: Comparison between the flow obtained from the LES simulation and the one resulted by the POD reconstruction

In figure 3.18 the energy spectra obtained during the POD analysis of 100 modes, corresponding to a time interval of 2 units of time[2]. It is noticeable that the more energetic modes are the ones closest to the vertical axis and the energy decreases while moving along the x axis. In this work the aim is to represent the velocity field using 50% of the total energy, therefore only the first 16 modes are analyzed. Table 3.5 shows the energy values for each mode and the percentage of energy, as the sum of the contributions from the previous modes, for the considered modes. Analyzing the velocity component along the flow, the energy can be expressed also as the turbulent kinetic energy. The turbulence is more present in the x-z direction so the contribution in energy is higher along this direction and represents almost all the energy of the system.

[2]In the non-dimensional analysis also the time has been nondimensionalized

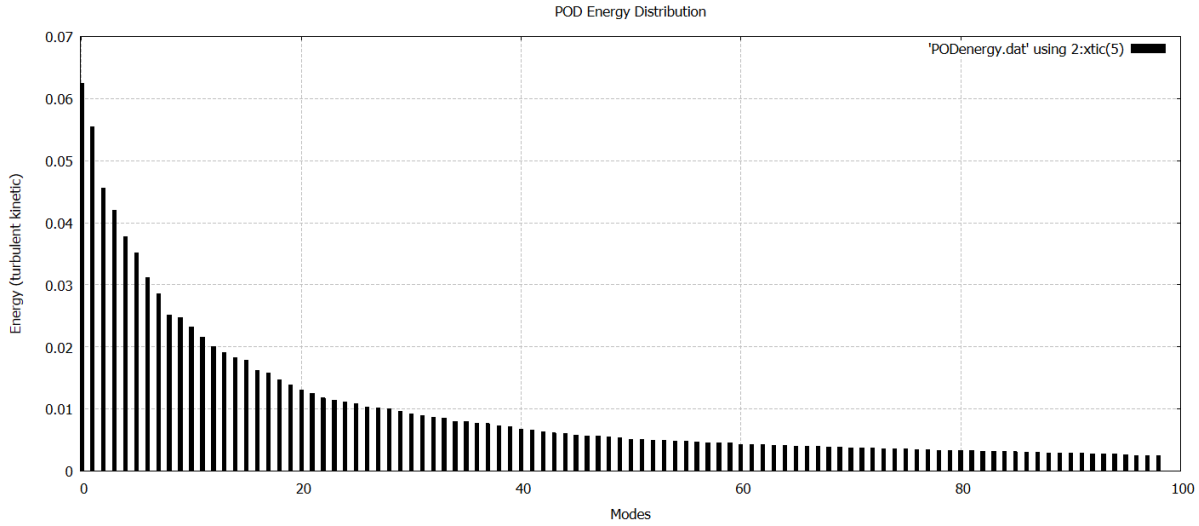

Figure 3.18: Energy spectra of the POD analysis using 100 modes. On the y axis there is the energy contribution in hundredths: the sum of all contributions is 1, which represents 100% of the energy.

Mode	Energy Contribution	Percentage
1	6.25×10^{-2}	6.25
2	5.54×10^{-2}	11.79
3	4.56×10^{-2}	16.36
4	4.20×10^{-2}	20.56
5	3.78×10^{-2}	24.34
6	3.51×10^{-2}	27.85
7	3.12×10^{-2}	30.97
8	2.85×10^{-2}	33.82
9	2.51×10^{-2}	36.33
10	2.48×10^{-2}	38.81
11	2.32×10^{-2}	41.13
12	2.16×10^{-2}	43.28
13	2.00×10^{-2}	45.28
14	1.91×10^{-2}	47.20
15	1.83×10^{-2}	49.03
16	1.79×10^{-2}	50.81

Table 3.5: Energy contributions for the first 16 modes and relative sum of the contributions from the previous modes.Values obtained by the POD analysis of 100 snapshots of the velocity field.

Figure 3.19 shows the time coefficients of each mode in the time interval considered. Time coefficients represent the energetic contribution of each mode over time. The followed trend is not smooth: the presence of fluid structures of multiple frequencies affects this time trace making it noisy.

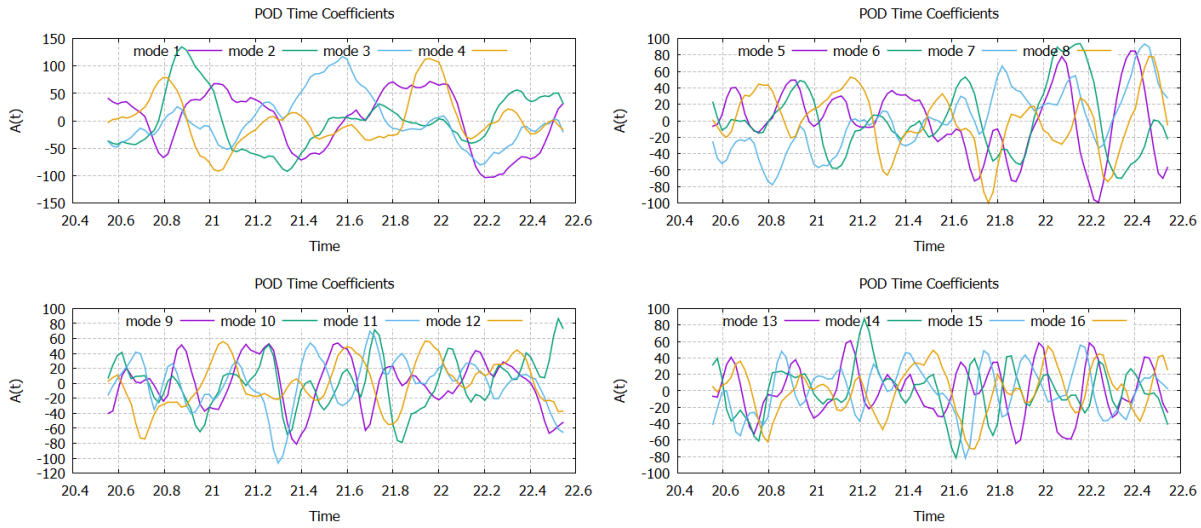

Figure 3.19: Time coefficients of the first 16 modes.

In figures 3.20 and 3.21, a comparison between the first six modes of the Mach 2 and Mach 5 POD analysis is shown. The modes are dimensionless and what is shown is the energetic distribution in the flow, using the same scale for both figures. The first thing that catches the eye is that, in the second figure, a portion of the energy is present in the front of the capsule, contrary to the Mach 2 case where the energy is concentrated. This observation is in line with what is stated in the discussion above, regarding fluctuation present in the Mach 5 fields.
Another difference can be observed looking at the area right behind the capsule. Here the wake results thicker in the first image, causing the wake to be wider than the one in the Mach 5 plots. The recirculating zone, represented as the area right behind the capsule, in the second figure, better follows the geometry of the body, assuming a more straight, conical shape that the bloated configuration of the Mach 2 recirculating area.
An aspect common to both the figure is that going from mode 1 to mode 6, the low frequencies become less visible. This is expected since the energy contributions decreases while and therefore, the more energetic high frequencies become more relevant.

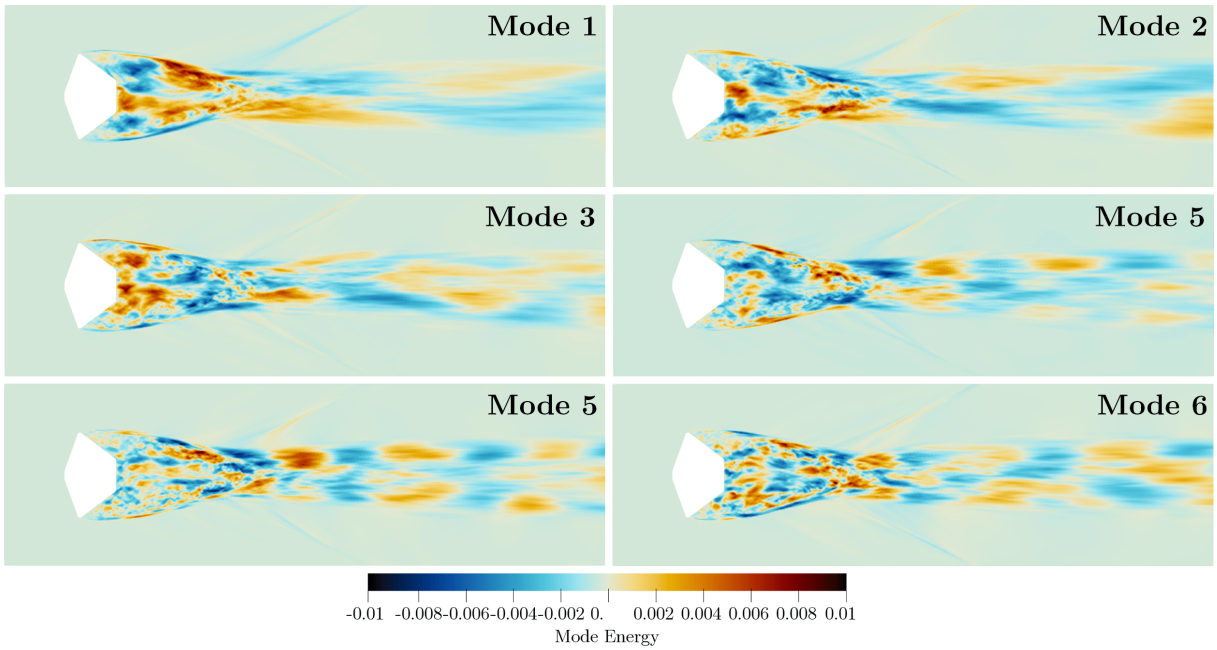

Figure 3.20: First six modes of the POD analysis for the Mach 2

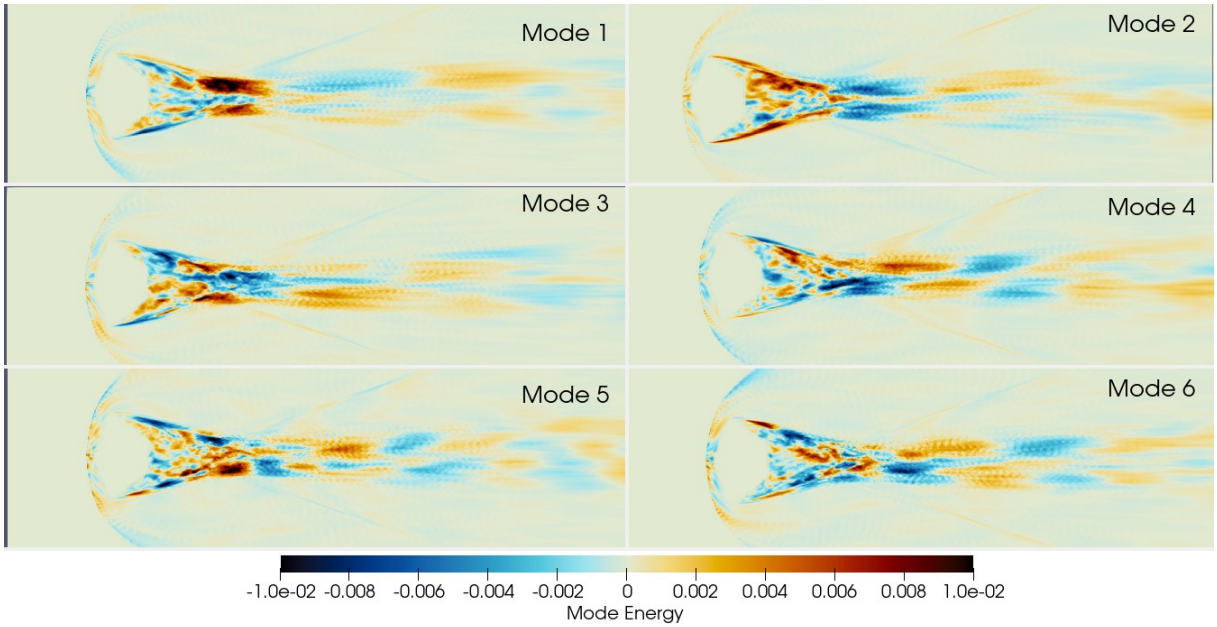

Figure 3.21: First six modes of the POD analysis for the Mach 5

Chapter 4

Conclusion

In this work the aerodynamical analysis of the flow around the ExoMars capsule in supersonic and hypersonic regimes with angle of attack 0° was carried out by simulating the flow at two different Mach conditions, 2 and 5. Both Mach numbers represent conditions that the capsule faces during the Entry, Descent and Landing phase, once it reaches Mars. Given the criticality of this phase for the success of the mission, the understanding of the aerodynamical phenomena that occur is fundamental.
The simulation was carried out using the Implicit Large Eddy Simulations, where only the larger eddies are simulated while the smaller vortexes are left to the numerical dissipation. This method allowed the implementation of the solver STREAmS [10] to carry out the simulations on CINECA's MARCONI100 cluster. The boundary conditions were imposed using the Immersed Boundary Method [13] featuring a grid of about 10^9 nodes.
Once the results were obtained, the values of the abrupted variations of density, pressure and temperature between the upstream and downstream of the wave, were checked using the Shock Expansion Theory.
In the end, the Proper Orthogonal Decomposition (POD) analysis was carried out to better understand the turbulent flow behind the capsule.
From the discussion of the results, the following observations can be extrapolated:

- as expected, with the increasing of the velocity, the shock wave moves closer to the capsule and it close up more around the body
- looking at the vorticity, some instability can be seen in front of the capsule. This affects the other fields and, in particular, this influence is evident in the entropy field. Here, in the Mach 5 case, the non-zero entropy region is wider than the wake, where in the Mach 2 entropy field the non-zero value was found.
- the freestream conditions are never reached againbehind the shock when the upstream Mach number is 5. This is observable in the qualitative study section, where the mean Mach fields real compared with the expected flow characteristic [24]. In fact the expansion fan and the recompression line that should characterize the flow and are present in the mean Mach 2 field, are not observable in the Mach 5 one. This is a consequence of the instabilities discussed before.
- the temperature is higher at greater velocity. This result is expected because during the entry phase the aerodynamic drag is used to slow down the capsule: the kinetic energy is therefore converted in thermal energy by the excitation of the molecules that compose the atmosphere.

- from the POD analysis, the turbulent region after the body turns out to be wider and more energetic in the Mach 2 case. Therefore, can be concluded that the turbulence is more intense when the Mach number is lower. The POD analysis shows, in addiction, a turbulent region in front of the capsule for Mach 5 flow. This observation is in line with the instabilities discussed above.

Even though these results help to shed a light on the aerodynamical behavior of the flow around a capsule in supersonic and hypersonic conditions, they are not enough to give full knowledge of the phenomenon. For instance, in this work the data collected where still not enough to obtain a meaningful trend of the drag and lift coefficients and only the zero degree angle of attack configuration was considered. Future works could start from here, continuing the work done in order to understand the behavior of these coefficients, or repeating the analysis for different angle of attack and Mach number. To improve the quality of the analysis, a wall model could be implemented, using WMLES instead of the LES method. By doing so the simulation would take into account also the drag produced by the viscous effects which are neglected in this work. Another change could be improving the subgrid model, which for now is assigned to the numerical dissipation.

Bibliography

[1] Agency, European Space. *ExoMars: Exploring Mars for evidence of Life*. URL: https://www.cosmos.esa.int/web/psa/exomars.

[2] Agency, European Space. *Schiaparelli landing investigation completed*. URL: https://www.esa.int/Science_Exploration/Human_and_Robotic_Exploration/Exploration/ExoMars/Schiaparelli_landing_investigation_completed.

[3] Agency, European Space. *The hazards of landing on Mars*. URL: https://exploration.esa.int/web/mars/-/58307-the-hazards-of-landing-on-mars.

[4] Agency, European Space. *The hazards of landing on Mars*. URL: https://exploration.esa.int/web/mars/-/58307-the-hazards-of-landing-on-mars.

[5] Agency, European Space. *Why go to Mars?* URL: https://www.esa.int/Science_Exploration/Human_and_Robotic_Exploration/Exploration/Why_go_to_Mars.

[6] Agency, Japan Aerospace Exploration. *About Orbital Re-entry Experiment (OREX)*. URL: https://global.jaxa.jp/projects/rockets/orex/index.html.

[7] Anderson, John. *EBOOK: Fundamentals of Aerodynamics (SI units)*. McGraw Hill, 2011.

[8] Anderson Jr, John D. *Hypersonic and High-Temperature Gas Dynamics*. 2006.

[9] Ball, Andrew J. et al. "The ExoMars Schiaparelli Entry, Descent and Landing Demonstrator Module (EDM) System Design". In: *Space Science Reviews* 218.5 (2022), p. 44.

[10] Bernardini, Matteo et al. "STREAmS: A high-fidelity accelerated solver for direct numerical simulation of compressible turbulent flows". In: *Computer Physics Communications* 263 (2021), p. 107906. ISSN: 0010-4655. DOI: https://doi.org/10.1016/j.cpc.2021.107906. URL: https://www.sciencedirect.com/science/article/pii/S0010465521000473.

[11] Bhandari, Pradeep and Anderson, Kevin R. "CFD Analysis For Assessing The Effect Of Wind On The Thermal Control Of The Mars Science Laboratory Curiosity Rover". In: *43rd International Conference on Environmental Systems*. DOI: 10.2514/6.2013-3325. eprint: https://arc.aiaa.org/doi/pdf/10.2514/6.2013-3325. URL: https://arc.aiaa.org/doi/abs/10.2514/6.2013-3325.

[12] Brandis, AM et al. "Simulation of the Schiaparelli Entry and Comparison to Aerosciences Flight Data". In: *Journal of Spacecraft and Rockets* 59.1 (2022), pp. 166–177.

[13] De Vanna, Francesco. "A high-resolution fully compressible Navier-Stokes solver for analysis of moving objects at high Mach numbers". PhD thesis. Università degli Studi di Padova, 2018.

[14] Edquist, Karl T et al. "Mars science laboratory entry capsule aerothermodynamics and thermal protection system". In: *2007 IEEE Aerospace Conference*. IEEE. 2007, pp. 1–13.

[15] Ferri, F et al. "Atmospheric mars entry and landing investigations & analysis (AMELIA) by ExoMars 2016 Schiaparelli Entry Descent module: The ExoMars entry, descent and landing science". In: *2017 IEEE International Workshop on Metrology for AeroSpace (MetroAeroSpace)*. IEEE. 2017, pp. 262–265.

[16] Gülhan, Ali et al. "Aerothermal measurements from the ExoMars Schiaparelli capsule entry". In: *Journal of Spacecraft and Rockets* 56.1 (2019), pp. 68–81.

[17] Gupta, Roop N, Lee, Kam-Pui, and Zoby, Ernest V. "Enhancements to viscous-shock-layer technique". In: *Journal of Spacecraft and Rockets* 30.4 (1993), pp. 404–413.

[18] Haas, Brian and Venkatapathy, Ethiraj. "Mars Pathfinder computations including base-heating predictions". In: *30th Thermophysics Conference*. 1995, p. 2086.

[19] Heppenheimer, Thomas A. *Facing the heat barrier: a history of hypersonics*. Vol. 4232. Government Printing Office, 2009.

[20] Hollis, Brian Ray. *Experimental and computational aerothermodynamics of a Mars entry vehicle*. North Carolina State University, 1996.

[21] Hornung, Hans G, Schramm, Jan Martinez, and Hannemann, Klaus. "Hypersonic flow over spherically blunted cone capsules for atmospheric entry. Part 1. The sharp cone and the sphere". In: *Journal of Fluid Mechanics* 871 (2019), pp. 1097–1116.

[22] Horvath, Thomas, McGinley, Catherine, and Hannemann, Klaus. "Blunt body near-wake flow field at Mach 6". In: *Fluid Dynamics Conference*. 1996, p. 1935.

[23] Liné, A. et al. "On POD analysis of PIV measurements applied to mixing in a stirred vessel with a shear thinning fluid". In: *Chemical Engineering Research and Design* 91.11 (2013), pp. 2073–2083.

[24] Mehta, RC. "Numerical simulation of supersonic flow past reentry capsules". In: *Shock Waves* 15.1 (2006), pp. 31–41.

[25] Mitcheltree, Robert and Gnoffo, Peter. "Wake flow about a MESUR Mars entry vehicle". In: *6th Joint Thermophysics and Heat Transfer Conference*. 1994, p. 1958.

[26] Mitcheltree, Robert A. "Aerothermodynamic methods for a Mars environmental survey Mars entry". In: *Journal of Spacecraft and Rockets* 31.3 (1994), pp. 516–523.

[27] Mittal, Rajat and Iaccarino, Gianluca. "Immersed boundary methods". In: *Annu. Rev. Fluid Mech.* 37 (2005), pp. 239–261.

[28] NASA. *Mars Exploration, Program and Mission*. URL: https://mars.nasa.gov/programmissions/overview/.

[29] NASA. *Mars Exploration Program, Historical Log*. URL: https://mars.nasa.gov/mars-exploration/missions/historical-log/.

[30] Pope, Stephen B and Pope, Stephen B. *Turbulent flows*. Cambridge university press, 2000.

[31] Shahriar, Al. "Study and Simulation of Inviscid Supersonic Flow over a Bluff Body". PhD thesis. May 2015. DOI: 10.13140/RG.2.1.3649.7765/2.

[32] Shimshi, Jason and Walberg, Gerald. "An investigation of aerodynamic heating to spherically blunted conesat angle of attack". In: *28th Thermophysics Conference*. 1992, p. 2764.

[33] Stewart, David and Chen, Y. "Convective heat-transfer rate distributions over a 140 deg blunt cone at hypersonic speeds in different gas environments". In: *28th Thermophysics Conference*. 1993, p. 2787.

[34] Taira, Kunihiko et al. "Modal analysis of fluid flows: An overview". In: *Aiaa Journal* 55.12 (2017), pp. 4013–4041.

Acknowledgement

I would like to thank my primary supervisor, Professor Francesco Picano, who assisted me during this project.
I would like to extent my thanks to my co-advisors Michele Cogo and Luca Placco for their support and for always being ready to give me the right suggestions.
My heartfelt thanks to my family, who supported and believed in me throughout my university career.
I would also like to thank my boyfriend who has been there for me when I needed it.
A special thank you goes to all my friends, both Italian and non, which made my university years unforgettable.